In conclusion, we generated antibody fragments with high affinity and specificity for gold nanoparticle surfaces by a one-pot procedure involving integration of peptide-grafting and phage-display techniques. The resulting antibody fragment suppressed the aggregation of gold nanoparticles even in a high-ionic-strength solution, and multivalent and bispecific antibody fragments based on the gold-binding VHH could be used to selectively contact gold nanoparticles with cells displaying the EGFR receptor, as well as to spontaneously link two different nanomaterials (gold−gold, gold−ZnO). We describe the utilization of high affinitive material-binding antibody fragments for one-pot functionalization of gold nanoparticles.

■ ASSOCIATED CONTENT

Supporting Information

Additional figures for the frequencies of amino acids in randomized CDR3 loop of VHH_{GBP1} and the size-exclusion chromatography for E32 tetramer. This material is available free of charge via the Internet at http://pubs.acs.org.

■ AUTHOR INFORMATION

Corresponding Author

*Tel and fax: +81-22-795-7276. E-mail: mitsuo@kuma.che.tohoku.ac.jp.

Notes

The authors declare no competing financial interest.

■ ACKNOWLEDGMENTS

This work was supported by a Scientific Research Grant from the Ministry of Education, Science, Sports, and Culture of Japan (M.U. and I.K.), by Precursory Research for Embryonic Science and Technology from the Japan Science and Technology Agency (JST, M.U.), and JSPS research fellowships for young scientists (T.H.).

■ ABBREVIATIONS

BSA, bovine serum albumin; CAnIGET, construction of antibodies by integrating grafting and evolution technology; CDR, complementarity determining regions; EGFR, epidermal growth factor receptor; GBP, gold-binding peptide; SPR, surface plasmon resonance; VHH, variable domain of the heavy chain of a heavy chain camel antibody

■ REFERENCES

(1) Chan, W. C. W., and Nie, S. (1998) Quantum Dot Bioconjugates for Ultrasensitive Nonisotopic Detection. *Science 281*, 2016−2018.

(2) Cao, Y., Jin, R., and Mirkin, C. (2002) Nanoparticles with Raman spectroscopic fingerprints for DNA and RNA detection. *Science 297*, 1536−1540.

(3) Joo, S. H., Choi, S. J., Oh, I., Kwak, J., Liu, Z., Terasaki, O., and Ryoo, R. (2001) Ordered nanoporous arrays of carbon supporting high dispersions of platinum nanoparticles. *Nature 412*, 169−172.

(4) Caruso, F., Caruso, R. A., and Möhwald, H. (1998) Nanoengineering of inorganic and hybrid hollow spheres by colloidal templating. *Science 282*, 1111−1114.

(5) Gao, X., Cui, Y., Levenson, R. M., Chung, L. W. K., and Nie, S. (2004) In vivo cancer targeting and imaging with semiconductor quantum dots. *Nat. Biotechnol. 22*, 969−976.

(6) Mornet, S., Vasseur, S., Grasset, F., and Duguet, E. (2004) Magnetic nanoparticle design for medical diagnosis and therapy. *J. Mater. Chem. 14*, 2161−2175.

(7) Zhang, J., Ohara, S., Umetsu, M., Naka, T., Hatakeyama, Y., and Adschiri, T. (2007) Colloidal Ceria Nanocrystals: A Tailor-made Crystal Morphology in Supercritical Water. *Adv. Mater. 19*, 203−206.

(8) Shevchenko, E. V., Talapin, D. V., Kotov, N. A., O'Brien, S., and Murray, C. B. (2006) Structural diversity in binary nanoparticle superlattices. *Nature 439*, 55−59.

(9) Whaley, S. R., English, D. S., Hu, E. L., Barbara, P. E., and Belcher, A. M. (2000) Selection of peptides with semiconductor binding specificity for directed nanocrystal assembly. *Nature 405*, 665−668.

(10) Sarikaya, M., Tamerler, C., Jen, A. K-Y., Schulten, K., and Baneyx, F. (2003) Molecular biomimetics: nanotechnology through biology. *Nat. Mater. 2*, 577−585.

(11) Naik, R. R., Stringer, S. J., Agarwal, G., Jones, S. E., and Stone, M. O. (2002) Biomimetic synthesis and patterning of silver nanoparticles. *Nat. Mater. 1*, 169−172.

(12) Mao, C., Solis, D. J., Reiss, B. D., Kottmann, S. T., Sweeney, R. Y., Hayhurst, A., Georgiou, G., Iverson, B., and Belcher, A. M. (2004) Virus-based toolkit for the directed synthesis of magnetic and semiconducting nanowires. *Science 303*, 213−217.

(13) Shimada, Y., Suzuki, M., Sugiyama, M., Kumagai, I., and Umetsu, M. (2011) Bioassisted capture and release of nanoparticles on nano-lithographed ZnO films. *Nanotechnology 22*, 275302(1−6).

(14) Park, T. J., Lee, S. Y., Lee, S. J., Park, J. P., Yang, K. S., Lee, K. B., Ko, S., Park, J. B., Kim, T., Kim, S. K., Shin, Y. B., Chung, B. H., Ku, S. J., Kim do, H., and Choi, I. S. (2006) Protein nanopatterns and biosensors using gold binding polypeptide as a fusion partner. *Anal. Chem. 78*, 7197−7205.

(15) Zhou, W., Schwartz, D. T., and Baneyx, F. (2010) Single-pot biofabrication of zinc sulfide immuno-quantum dots. *J. Am. Chem. Soc. 132*, 4731−4738.

(16) Umetsu, M., Mizuta, M., Tsumoto, K., Ohara, S., Takami, S., Watanabe, H., Kumagai, I., and Adschiri, T. (2005) Bioassisted room-temperature immobilization and mineralization of zinc oxide - the structural ordering of ZnO nanoparticles into a flower-type morphology. *Adv. Mater. 17*, 2571−2575.

(17) Kramer, R. M., Li, C., Carter, D. C., Stone, M. O., and Naik, R. R. (2004) Engineered Protein Cages for Nanomaterial Synthesis. *J. Am. Chem. Soc. 126*, 13282−13286.

(18) Chiu, C.-Y., Li, Y., Ruan, L., Ye, X., Murray, C. B., and Huang, Y. (2011) Platinum nanocrystals selectively shaped using facet-specific peptide sequences. *Nat. Chem. 3*, 393−399.

(19) Ibii, T., Kaieda, M., Hatakeyama, S., Shiotuka, H., Kumagai, I., Watanabe, H., Umetsu, M., and Imamura, T. (2010) Direct immobilization of gold-binding antibody fragments for immunosensor applications. *Anal. Chem. 82*, 4229−4235.

(20) Hattori, T., Umetsu, M., Nakanishi, T., Togashi, T., Yokoo, N., Abe, H., Ohara, S., Adschiri, T., and Kumagai, I. (2010) High affinity anti-inorganic material antibody generation by integrating graft and evolution technologies. Potential of antibodies as biointerface molecules. *J. Biol. Chem. 285*, 7784−7793.

(21) Bogan, A. A., and Thorn, K. S. (1998) Anatomy of hot spots in protein interfaces. *J. Mol. Biol. 280*, 1−9.

(22) Li, Y., Li, H., Yang, F., Smith-Gill, S. J., and Mariuzza, R. A. (2003) X-ray snapshots of the maturation of an antibody response to a protein antigen. *Nat. Struct. Biol. 10*, 482−488.

(23) Hattori, T., Umetsu, M., Nakanishi, T., Tsumoto, K., Ohara, S., Abe, H., Naito, M., Asano, R., Adschiri, T., and Kumagai, I. (2008) Grafting of material-binding function into antibodies: functionalization by peptide grafting. *Biochem. Biophys. Res. Commun. 365*, 751−757.

(24) Watanabe, H., Nakanishi, T., Umetsu, M., and Kumagai, I. (2008) Human anti-gold antibodies: Biofunctionalization of gold nanoparticles and surfaces with anti-gold antibodies. *J. Biol. Chem. 283*, 36031−38.

(25) Mirkin, C. A., Letsinger, R. L., Mucic, R. C., and Storhoff, J. J. (1996) A DNA-based method for rationally assembling nanoparticles into macroscopic materials. *Nature 382*, 607−609.

(26) El-Sayed, I. H., Huang, X., and El-Sayed, M. A. (2005) Surface plasmon resonance scattering and absorption of anti-EGFR antibody conjugated gold nanoparticles in cancer diagnostics: applications in oral cancer. *Nano Lett. 5*, 829−834.

(27) Huang, J.-S., Callegari, V., Geisler, P., Brüning, C., JKern, J., Prangsma, J. C., Wu., X., Feichtner, T., Ziegler, J., Weinmann, P., Kamp, M., Forchel, A., Biagioni, P., Sennhauser, U., and Hecht, B. (2010) Atomically flat single-crystalline gold nanostructures for plasmonic nanocircuitry. *Nat. Commun. 1*, 150(1−8).
(28) Nam, K. T., Kim, D. W., Yoo, P. J., Chiang, C. Y., Meethong, N., Hammond, P. T., Chiang, Y. M., and Belcher, A. M. (2006) Virus-enabled synthesis and assembly of nanowires for lithium ion battery electrodes. *Science 312*, 885−888.
(29) Maenaka, K., Furuta, M., Tsumoto, K., Watanabe, K., Ueda, Y., and Kumagai, I. (1996) A stable phage-display system using a phagemid vector: phage display of hen egg-white lysozyme (HEL), Escherichia coli alkaline, phosphatase, and anti-HEL monoclonal antibody, HyHEL10. *Biochem. Biophys. Res. Commun. 218*, 682−687.
(30) Roovers, R. C., Laeremans, T., Huang, L., De Taeye, S., Verkleij, A. J., Revets, H., De Haard, H. J., and Van Bergen En Henegouwen, P. M. P. (2007) Efficient inhibition of EGFR signalling and of tumour growth by antagonistic anti-EGFR nanobodies. *Cancer Immunol. Immunother. 56*, 303−317.
(31) Conrath, K., Lauwereys, M., Wyns, L., and Muyldermans, S. (2001) Camel single-domain antibodies as modular building units in bispecific and bivalent antibody constructs. *J. Biol. Chem. 276*, 7346−7350.
(32) Cloutier, S. M., Couty, S., Terskikh, A., Marguerat, L., Crivelli, V., Pugnières, M., Mani, J., Leisinger, H., Mach, J., and Deperthes, D. (2000) Streptabody, a high avidity molecule made by tetramerization of in vivo biotinylated, phage display-selected scFv fragments on streptavidin. *Mol. Immunol. 37*, 1067−1077.
(33) Saerens, D., Pellis, M., Loris, R., Pardon, E., Dumoulin, M., Matagne, A., Wyns, L., Muyldermans, S., and Conrath, K. (2005) Identification of a universal VHH framework to graft non-canonical antigen-binding loops of camel single-domain antibodies. *J. Mol. Biol. 352*, 597−607.
(34) Yokoo, N., Togashi, T., Umetsu, M., Tsumoto, K., Hattori, T., Nakanishi, T., Ohara, S., Takami, S., Naka, T., Abe, H., Kumagai, I., and Adschiri, T. (2010) Direct and selective immobilization of proteins by means of an inorganic material-binding peptide: discussion on functionalization in the elongation to material-binding peptide. *J. Phys. Chem. B 114*, 480−486.
(35) Krämer, S., Xie, H., Gaff, J., Williamson, J. R., Tkachenko, A. G., Nouri, N., Feldheim, D. A., and Feldheim, D. L. (2004) Preparation of protein gradients through the controlled deposition of protein-nanoparticle conjugates onto functionalized surfaces. *J. Am. Chem. Soc. 126*, 5388−5395.
(36) Burt, J. L., Gutiérrez-Wing, C., Miki-Yoshida, M., and José-Yacamán, M. (2004) Noble-metal nanoparticles directly conjugated to globular proteins. *Langmuir 20*, 11778−11783.
(37) Adams, G. P., and Weiner, L. M. (2005) Monoclonal antibody therapy of cancer. *Nat. Biotechnol. 23*, 1147−1157.
(38) Sharkey, R. M., Cardillo, T. M., Rossi, E. A., Chang, C. H., Karacay, H., McBride, W. J., Hansen, H. J., Horak, I. D., and Goldenberg, D. M. (2005) Signal amplification in molecular imaging by pretargeting a multivalent, bispecific antibody. *Nat. Med. 11*, 1250−1255.
(39) Barbas, C. F., Rosenblum, J., and Lerner, R. (1993) Direct selection of antibodies that coordinate metals from semisynthetic combinatorial libraries. *Proc. Natl. Acad. Sci. U.S.A. 90*, 6385−6389.
(40) Schnirman, A. A., Zahavi, E., Yeger, H., Rosenfeld, R., Benhar, I., Reiter, Y., and Sivan, U. (2006) Antibody molecules discriminate between crystalline facets of a gallium arsenide semiconductor. *Nano Lett. 6*, 1870−1874.
(41) Barbas, C. F., Languino, L. R., and Smith, J. W. (1993) High-affinity self-reactive human antibodies by design and selection: Targeting the integrin ligand binding site. *Proc. Natl. Acad. Sci. U.S.A. 90*, 10003−10007.
(42) Peelle, B. R., Krauland, E. M., Wittrup, K. D., and Belcher, A. M. (2005) Design criteria for engineering inorganic material-specific peptides. *Langmuir 21*, 6929−6933.
(43) Holliger, P., and Hudson, P. J. (2005) Engineered antibody fragments and the rise of single domains. *Nat. Biotechnol. 23*, 1126−1136.
(44) Watanabe, H., Kanazaki, K., Nakanishi, T., Shiotsuka, H., Hatakeyama, S., Kaieda, M., Imamura, T., Umetsu, M., and Kumagai, I. (2011) Biomimetic engineering of modular bispecific antibodies for biomolecule immobilization. *Langmuir 27*, 9656−9661.
(45) Ward, E. S., Güssow, D., Griffiths, A. D., Jones, P. T., and Winter, G. (1989) Binding activities of a repertoire of single immunoglobulin variable domains secreted from Escherichia coli. *Nature 341*, 544−546.
(46) Derjaguin, B. V., and Landau, L. (1941) Theory of the stability of strongly charged lyophobic sols and of the adhesion of strongly charged particles in solutions of electrolytes. *Acta Physicochim. URSS 14*, 633−662.
(47) Verwey, E. J. W. (1947) Theory of the stability of lyophobic colloids. *J. Phys. Colloid Chem. 51*, 631−636.
(48) Daniel, M. C., and Astruc, D. (2004) Gold nanoparticles: assembly, supramolecular chemistry, quantum-size-related properties, and applications toward biology, catalysis, and nanotechnology. *Chem. Rev. 104*, 293−346.
(49) Norde, W. (1986) Adsorption of proteins from solution at the solid-liquid interface. *Adv. Colloid Interface Sci. 25*, 267−340.
(50) Lucocq, J. (1994) Quantitation of gold labelling and antigens in immunolabelled ultrathin sections. *J. Anat. 184*, 1−13.
(51) Mayhew, T. M., Muhlfeld, C., Vanhecke, D., and Ochs, M. (2009) A review of recent methods for efficiently quantifying immunogold and other nanoparticles using TEM sections through cells, tissues and organs. *Ann. Anat. 191*, 153−170.
(52) El-Sayed, I. H., Huang, X., and El-Sayed, M. A. (2006) Selective laser photo-thermal therapy of epithelial carcinoma using anti-EGFR antibody conjugated gold nanoparticles. *Cancer Lett. 239*, 129−135.
(53) Jones, M. R., Macfarlane, R. J., Lee, B., Zhang, J., Young, K. L., Senesi, A. J., and Mirkin, C. A. (2010) DNA-nanoparticle superlattices formed from anisotropic building blocks. *Nat. Mater. 9*, 913−917.
(54) Connolly, S., Fitzmaurice, D. S., and Connolly, D. (1999) Fitzmaurice, Programmed assembly of gold nanocrystals in aqueous solution. *Adv. Mater. 11*, 1202−1205.
(55) Dimitrijevic, N. M., Saponjic, Z. V., Rabatic, B. M., and Rajh, T. (2005) Assembly and charge transfer in hybrid TiO_2 architectures using biotin-avidin as a connector. *J. Am. Chem. Soc. 127*, 1344−1345.
(56) Shenton, W., Davis, S. A., and Mann, S. (1999) Directed self-assembly of nanoparticles into macroscopic materials using antibody−antigen recognition. *Adv. Mater. 11*, 449−452.
(57) Kacar, T., Ray, J., Gungormus, M., Oren, E. E., Tamerler, C., and Sarikaya, M. (2009) Quartz binding peptides as molecular linkers towards fabricating multifunctional micropatterned substrates. *Adv. Mater. 21*, 295−299.
(58) Wei, J. H., Kacar, T., Tamerler, C., Sarikaya, M., David, S., and Ginger, D. S. (2009) Nanopatterning peptides as bifunctional inks for templated assembly. *Small 5*, 689−693.

Materials Letters 79 (2012) 78–80

Contents lists available at SciVerse ScienceDirect

Materials Letters

journal homepage: www.elsevier.com/locate/matlet

Directed assembly of metal oxide nanoparticles by DNA

Jinghua Han [a,b], Satoshi Ohara [a,*], Kazuyoshi Sato [c], Hui Xu [d], Zhenquan Tan [a], Yoshiaki Morisada [a], Kazuo Kuruma [a], Makio Naito [a], Ping Shan [b], Mitsuo Umetsu [e]

[a] Joining and Welding Research Institute, Osaka University, 11-1 Mihogaoka, Ibaraki, Osaka 567-0047, Japan
[b] School of Material Science and Engineering, Tianjin University, No.92, Weijin Road, Nankai District, Tianjin City 300072, China
[c] Department of Chemical & Environmental Engineering, Graduate School of Engineering, Gunma University, 1-5-1 Tenjin-cho, Kiryu, Gunma 376-8515, Japan
[d] School of Pharmacy, Shenyang Pharmaceutical University, No.103, Wenhua Road, Shenhe District, Shenyang City, Liaoning Province, China
[e] Department of Biomolecular Engineering, Graduate School of Engineering, Tohoku University, 6-6-11 Aoba, Aramaki, Aoba-ku, Sendai, Miyagi 980-8579, Japan

ARTICLE INFO

Article history:
Received 28 December 2011
Accepted 24 March 2012
Available online 31 March 2012

Keywords:
Assembly
Zirconia
Nanoparticles
DNA

ABSTRACT

Directed assembly of metal oxide nanoparticles with the aid of DNA was investigated. One-dimensional arrangement of zirconia (ZrO_2) nanoparticles using DNA as a template was shown by TEM observation. It is considered that the DNA-directed assembly of ZrO_2 nanoparticles is due to the Coulomb interactions between the negatively charged DNA and positively charged ZrO_2 nanoparticles.

1. Introduction

When used as building blocks for nanostructures, nanoparticles make further miniaturization of structures and devices possible [1]. Recently assembling nanoparticles on the nanoscale has received considerable attention [2–11], and one tool for creating these assemblies is biomaterials. Deoxyribonucleic acid (DNA) is an appropriate biopolymer template for constructing defined inorganic materials, and highly selective base-pairing interactions between complementary single-strand DNA chains have been used in nanoassemblies. Additionally, native double-helical DNA can directly interact with metal ions and their complexes, and the role of DNA in assembling metal nanoparticles has been reported [12–20]. Recently, assembly of metal oxide nanoparticles has been demonstrated by surfactant capping on the nanoparticles [21,22]. However, DNA-directed assembly of metal oxide nanoparticles remains a challenge.

Metal oxide ceramic nanoparticles have been extensively investigated due to their successful applications and potential in various fields such as electronics, catalysis, pharmaceutics, energy storage, and medical applications, and using DNA to assemble metal oxide nanoparticles may allow novel hybrid nano-biomaterials with synergetic properties and functions to be realized. Zirconia (ZrO_2) is an attractive ceramic material due to its excellent mechanical, tribological and thermal properties, and good oxygen ionic conductivity. Its nanoparticles have a broad range of applications, including thermal barrier coatings, solid-state electrolytes, solid oxide fuel cells, oxygen sensors, and heterogeneous catalysts etc. [23–29]. From the viewpoint of several key applications, the assembly of ZrO_2 ceramic nanoparticles has been eagerly anticipated. The aim of this communication is to elucidate the directed assembly of ZrO_2 nanoparticles with the aid of DNA. Herein, we show the first example of a one-dimensional arrangement of metal oxide nanoparticles without surfactant capping using DNA as a template.

2. Experimental

The ZrO_2 ceramic nanoparticles, which were synthesized by a hydrothermal reaction, were a colloidal solution. Aqueous solution of $ZrOCl_2 \cdot 8H_2O$ was mixed with $KHCO_3$/KOH solution. Then the solution was hydrothermally treated at 150 °C for 1 h in the Teflon lined stainless steel vessel. The detailed hydrothermal synthesis is described in a previously reported method [30]. After the reaction, ZrO_2 nanoparticles in the solution were purified by washing ten times with deionized water and 5 M of HCl was added to the product for dispersion of the nanoparticles in water. The particle size distribution of the obtained ZrO_2 nanoparticle colloidal solution was measured by the dynamic light scattering (DLS) method, whereas transmission electron microscopy (TEM) was used to observe the ZrO_2 nanoparticles and their assembled nanostructures.

Two types of DNA solutions were used in this study: λ-DNA and a short DNA fragment. The ZrO_2 nanoparticles were assembled by λ-DNA as follows. λ-DNA, which was 48,502 base-pairs (bp) long, was purchased from TaKaRa Biotechnology (Dalian) Co., Ltd. The original concentration

* Corresponding author. Tel./fax: +81 6 6879 4370.
E-mail address: ohara@jwri.osaka-u.ac.jp (S. Ohara).

0167-577X/$ – see front matter © 2012 Elsevier B.V. All rights reserved.
doi:10.1016/j.matlet.2012.03.094

was 0.3 μg/μL, and the equivalent base pair concentration was 450 μmol/L. The buffer was 10 mmol Tris–HCl–1 mmol EDTA, pH = 8.0, A260/A280 = 1.8–2.0 (DNA purity). A260 and A280 are the optical spectrometer measurement of absorbance at the wavelengths of 260 nm and 280 nm, respectively. The λ-DNA solution (450 μmol/L bp concentration) was diluted to a 1 μmol/L bp concentration by adding a 0.0025 mol/L HCl solution to maintain the pH of λ-DNA near 3.0. A 900 μL ZrO_2 solution (concentration 50 μmol/L) with a HCl solution was prepared to maintain a constant pH value of 3.0. Then 900 μL ZrO_2 solution was added to the 900 μL solution of 0.5 μmol/L bp λ-DNA to make a 1800 μL compound solution of 0.25 μmol/L bp λ-DNA.

The short DNA fragment, which was 50 bp linear and double-stranded, was purchased from Lonza Rockland Inc. To realize a pH of 3.0, the 100 μL short DNA fragment of 138.5 μmol/L was diluted ten-fold to a 1000 μL solution of 13.85 μmol/L with HCl solution (0.0025 mol/L). In the same manner, the zirconia solution (11.3 mmol/L) was diluted two thousand times with a HCl solution to make a 1000 μL solution with a zirconia concentration of 5.65 μmol/L. Then 1000 μL zirconia solution was added to the 1000 μL short DNA fragment solution to yield a mixed solution with a pH of 2.8. The absorption spectrum and zeta potential of DNA solutions were evaluated using an ultraviolet–visible (UV–vis) scanning spectrometer and a zeta potential analyzer, respectively.

3. Results and discussion

Fig. 1a and b shows a photograph and particle size distribution of the obtained transparent ZrO_2 colloidal solution. The ZrO_2 nanoparticle surface contains numerous positive charges at a pH value of 3 because the isoelectric point of ZrO_2 ceramic is around 5–6, and due to the electric repulsion force in water, each ZrO_2 nanoparticle is assumed to be dispersed separately. The average diameter of the ZrO_2 nanoparticle is about 5 nm, and has a very narrow particle distribution (Fig. 1b). Fig. 1c shows a TEM picture of the ZrO_2 nanoparticles. Although the primary ZrO_2 nanoparticles on the TEM grid aggregate after drying the colloidal solution, the primary nanoparticles are about 5 nm, which is consistent with that measured by DLS. Hence, it is concluded that the ZrO_2 nanoparticles can be dispersed perfectly in water under this low pH condition.

Fig. 2 shows the TEM picture of the mixed solution of ZrO_2 nanoparticles and λ-DNA, and indicates that a network is formed as the ZrO_2 nanoparticles are assembled on the DNA strands. In contrast, without DNA, the ZrO_2 nanoparticles are aggregated randomly on the TEM grid (Fig. 1c). However, the ZrO_2 nanoparticles are arranged in the presence of λ-DNA and the morphology agrees well with the assembly of metal nanoparticles by λ-DNA [13,20]. This TEM observation suggests that DNA plays an active role in the directed assembly process of ZrO_2 nanoparticles.

The length of the λ-DNA molecule is very long compared to the size of ZrO_2 ceramic nanoparticles. Thus, to confirm that the ZrO_2 nanoparticles are arranged on DNA, a short DNA fragment with a short length was used. 50 bp of the short DNA fragment corresponds to 17 nm, because the length of one bp is 0.34 nm. Fig. 3 shows the TEM picture of ZrO_2 nanoparticles assembled on the short DNA fragment, and illustrates that several ZrO_2 nanoparticles form an array on the short DNA. Although some ZrO_2 arrays aggregate each other, the ZrO_2 nanoparticles are aligned along the DNA template, as seen in Fig. 3, which reflects the linear morphology of the DNA.

The absorption spectrum and zeta potential of DNA in the working buffer were measured in order to consider the interaction between the DNA molecules and the ZrO_2 nanoparticles. It is thought that the short DNA fragment is stable in the acidic solution, because the absorption property around at 270 nm is not changed in comparison with that in the water. Then, it is confirmed that the short DNA fragment has negative charge even in the acidic solution. Futhermore, when the concentartion of the short DNA fragment increases, each ZrO_2 nanoparticle is individually observed on the TEM grid (Fig. 4). Therefore, the one-

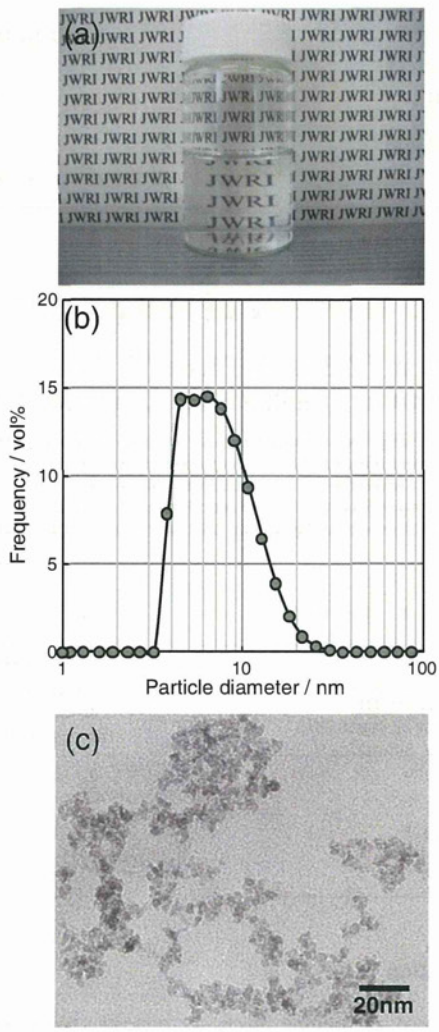

Fig. 1. (a) Photograph and (b) particle size distribution of the synthesized transparent zirconia nanoparticles in water. (c) TEM image of the synthesized zirconia nanoparticles.

dimensional (1D) arrangement is likely due to the Coulomb interactions between the negatively charged DNA and positively charged ZrO_2 nanoparticles.

To date, some groups have reported the assembly of metal oxide nanoparticles by DNA templates [21,22]. However, both nanoparticles were capped by surfactant such as tetramethylammonium hydroxide

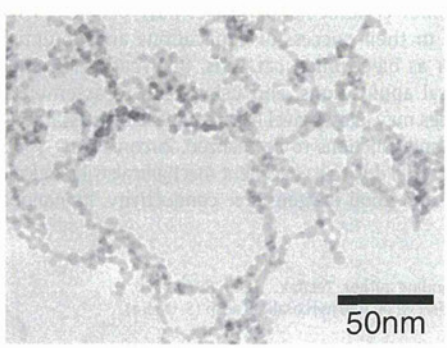

Fig. 2. TEM image of a zirconia nanoparticle assembly by λ-DNA.

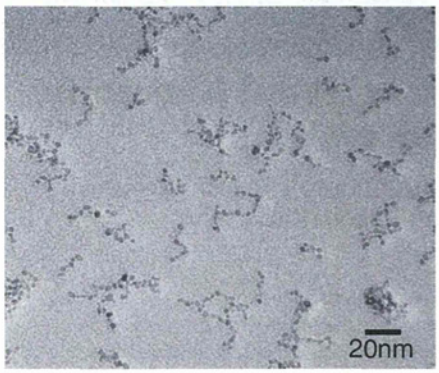

Fig. 3. TEM image of the zirconia nanoparticle assembly by a short DNA fragment. Concentration of the DNA is 13.85 μmol/L.

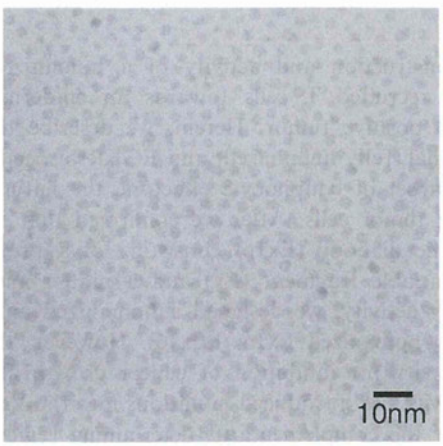

Fig. 4. TEM image of the zirconia nanoparticle assembly by a short DNA fragment. Concentration of the DNA is 138.5 μmol/L.

(TMAH) or cetyltrimethylammonium bromide (CTAB) in order to improve their dispersibility in solution, and the surfactant played an important role in assembling the nanoparticles on DNA. In contrast, the ZrO_2 nanoparticles used in this study are very stable in water without surfactant capping. Hence, we succeeded in DNA-directed assembly of metal oxide nanoparticles for the first time.

4. Conclusion

The role of DNA in assembling metal oxide nanoparticles without surfactant capping was investigated. ZrO_2 nanoparticles are assembled on DNA by Coulomb interactions between the negatively charged DNA and positively charged ZrO_2 nanoparticles. We believe that this directed assembly of metal oxide nanoparticles by DNA will yield novel hybrid nano-biomaterials with synergetic properties and functions.

Acknowledgment

This research was partly supported by a Scientific Research Grant and Grant-in-Aid for Cooperative Research Project of Advanced Materials Development and Integration of Novel Structured Metallic and Inorganic Materials from the Ministry of Education, Culture, Sports, Science and Technology of Japan.

References

[1] Schmid G, editor. Nanoparticles. Wiley-VCH Weinheim; 2004.
[2] Bae AH, Numata M, Hasegawa T, Li C, Kaneko K, Sakurai K, et al. Angew Chem Int Ed 2005;44:2030–3.
[3] Fu AH, Micheel CM, Cha J, Chang H, Yang H, Allivisatos AP. J Am Chem Soc 2004;126:10832–3.
[4] Nakao H, Shiigi H, Yamamoto Y, Tokonami S, Nagaoka T, Sugiyama S, et al. Nano Lett 2003;3:1391–4.
[5] Mirkin CA, Letsinger RL, Mucie RC, Storhoff JJ. Nature 1996;382:607–9.
[6] Sato K, Hosokawa K, Maeda M. J Am Chem Soc 2003;125:8102–3.
[7] Gu Q, Cheng C, Haynie DT. Nanotechnology 2005;16:1358–63.
[8] Braun E, Eichen Y, Sivan U, Ben-Yoseph G. Nature 1998;392:775–8.
[9] Zinchenko AA, Yoshikawa K, Baigl D. Adv Mater 2005;17:2820–3.
[10] Kumar A, Pattarkine M, Bhadbhade M, Mandale AB, Ganesh KN, Datar SS, et al. Adv Mater 2001;13:341–4.
[11] Xiao SJ, Liu FR, Rosen AE, Hainfeld JF, Seeman NC, Musier-Forsyth K, et al. J Nanopart Res 2002;4:313–7.
[12] Richter J, Merig M, Pompe W, Monch I, Schackert HK. Appl Phys Lett 2001;78:536–8.
[13] Richter J, Seidel R, Kirsch R, Mertig M, Pompe W, Plaschke J, et al. Adv Mater 2000;12:507–10.
[14] Ford WE, Harnack O, Yasuda A, Wessels JM. Adv Mater 2001;12:1793–7.
[15] Mertig M, Ciacchi LC, Seidel R, Pompe W, De Vita A. Nano Lett 2002;2:841–4.
[16] Keren K, Krueger M, Gilad R, Ben-Yoseph G, Sivan U, Braun E. Science 2002;297:72–5.
[17] Keren K, Berman RS, Braun E. Nano Lett 2004;4:323–6.
[18] Monson CF, Woolley AT. Nano Lett 2003;3:359–63.
[19] Becerril HA, Stoltenberg RM, Monson CF, Woolley AT. J Mater Chem 2004;14:611–6.
[20] Hatakeyama Y, Umetsu M, Ohara S, Kawadai F, Takami S, Naka T, et al. Adv Mater 2008;20:1122–8.
[21] Nyamjav D, Ivanisevic A. Biomaterials 2005;26:2749–57.
[22] Wang L, Wei G, Qi B, Zhou H, Liu Z, Song Y, et al. Appl Surf Sci 2006;252:2711–6.
[23] Ye Z, Tan M, Wang G, Yuan J. J Fluoresc 2005;15:499–505.
[24] Limaye AU, Helble JJ. J Am Ceram Soc 2002;85:1127–32.
[25] Schmidt T, Menning M, Schmidt H. J Am Ceram Soc 2007;90:1401–5.
[26] Trunec M, Maca K. J Am Ceram Soc 2007;90:2735–40.
[27] Shankar SS, Joshi H, Pasricha R, Pavaskar NR, Mandale AB, Sastry M. J Colloid Interface Sci 2004;269:126–30.
[28] Matsui K, Ohgai M. J Am Ceram Soc 2001;84:2303–12.
[29] Hannink RHJ, Kelly PM, Muddle BC. J Am Ceram Soc 2000;83:461–87.
[30] Sato K, Abe H, Ohara S. J Am Chem Soc 2010;13:2538–9.

the FEBS Journal

Construction and humanization of a functional bispecific EGFR × CD16 diabody using a refolding system

Ryutaro Asano[1], Makoto Nakayama[1], Hiroko Kawaguchi[1], Tsuguo Kubota[1], Takeshi Nakanishi[1], Mitsuo Umetsu[1], Hiroki Hayashi[2], Yu Katayose[2], Michiaki Unno[2], Toshio Kudo[3] and Izumi Kumagai[1]

1 Department of Biomolecular Engineering, Graduate School of Engineering, Tohoku University, Sendai, Japan
2 Division of Gastroenterological Surgery, Department of Surgery, Graduate School of Medicine, Tohoku University, Sendai, Japan
3 Cell Resource Center for Biomedical Research, Institute of Development, Aging, and Cancer, Tohoku University, Sendai, Japan

Keywords
bispecific diabody; cancer immunotherapy; CD16; epidermal growth factor receptor; humanization

Correspondence
Izumi Kumagai, Department of Biomolecular Engineering, Graduate School of Engineering, Tohoku University, Aoba 6-6-11-606, Aramaki, Aoba-ku, Sendai 980-8579, Japan
Fax: +81 22 795 6164
Tel: +81 22 795 7274
E-mail: kmiz@kuma.che.tohoku.ac.jp

(Received 10 February 2011, revised 4 November 2011, accepted 7 November 2011)

doi:10.1111/j.1742-4658.2011.08417.x

We previously reported the construction and activity of a humanized, bispecific diabody (hEx3) that recruited T cells towards an epidermal growth factor receptor (EGFR) positive tumor. Herein, we describe the construction of a second functional, fully humanized, anti-EGFR bispecific diabody that recruits another subset of lymphocyte effectors, the natural killer cells, to EGFR-expressing tumor cells. After we confirmed that an anti-EGFR × anti-CD16 bispecific diabody (Ex16) consisting of a previously humanized anti-EGFR variable fragment (Fv) and a mouse anti-CD16 Fv had growth inhibitory activity, we designed a humanized anti-CD16 Fv to construct the fully humanized Ex16 (hEx16). However, the humanized form had lower activity for inhibition of cancer growth. To restore its growth inhibitory activity, we introduced mutations into the Vernier zone, which is located near the complementarity-determining regions and is involved in their binding activity. We efficiently prepared 15 different hEx16 mutants by expressing each chimeric single-chain component for hEx16 separately. We then used our *in vitro* refolding system to select the most functional mutant, which had a growth inhibitory effect comparable with that of the commercially available chimeric anti-EGFR antibody, cetuximab. Our refolding system could aid in the efficient optimization of other proteins with heterodimeric structure.

Introduction

Bispecific antibodies (BsAbs) are recombinant antibodies that can bind to two different antigenic epitopes. Bispecificity can be used in cancer immunotherapy to crosslink tumor cells to immune cells such as cytotoxic T cells, natural killer (NK) cells and macrophages. This crosslinking accelerates the destruction of tumor cells by immune cells, which may translate into improved antitumor therapy and lower costs by decreasing the doses needed for therapy [1,2]. However, the use of BsAbs in clinical studies has been hampered by difficulties in producing them on a large scale. Conventional chemical conjugation results in inconsistent quality of the antibodies produced [3]. The production of BsAbs by somatic fusion of two

Abbreviations
ADCC, antibody-dependent cellular cytotoxicity; BsAbs, bispecific antibodies; CDR, complementarity-determining regions; CHO, Chinese hamster ovary; CTLs, cytotoxic T lymphocytes; EGFR, epidermal growth factor receptor; FITC, fluorescein isothiocyanate; Fv, variable fragment; MHC, major histocompatibility complex; MTS, 3-(4,5-dimethylthiazole-2-yl)-5-(3-carboxymethoxyphenyl)-2-(4-sulfophenyl)-2*H*-tetrazolium, inner salt; NK, natural killer; NK-LAK, lymphokine-activated killer cells with the NK cell phenotype; PBMCs, peripheral blood mononuclear cells; SPR, surface plasmon resonance; TCR, T cell receptor; T-LAK, lymphokine-activated killer cells with the T-cell phenotype.

hybridomas to form a quadroma yields BsAbs of more consistent quality, but this results in the formation of various chain-shuffled antibodies. For instance, 10 different antibodies can be generated after random association of two heavy and two light chains [4,5].

Advances in recombinant DNA technology have made it feasible to generate small recombinant BsAb fragments constructed from two different variable antibody fragments. Bispecific diabodies are the smallest available BsAb fragments and the distance between the two antigen binding sites is sufficient to link two cells [6,7]. The effectiveness of bispecific diabodies in cancer therapy has been extensively shown in both *in vitro* and *in vivo* models [8–10]. We have constructed functional bispecific diabodies [11,12] and have reported that a humanized bispecific diabody, hEx3, has marked antitumor activity and can retarget lymphokine-activated killer cells with the T-cell phenotype (T-LAK cells) against epidermal growth factor receptor (EGFR) positive cell lines [13,14].

Among immune cells, cytotoxic T lymphocytes (CTLs) are one of the most suitable candidates for targeted immunotherapy, as they participate in the recognition and subsequent killing of tumor cells, virus-infected cells and allogeneic targets [1]. The primary cytotoxic trigger on CTLs is the cluster of differentiation 3/T-cell receptor (CD3–TCR) complex, which is antigen-specific but is restricted by the major histocompatibility complex (MHC). However, BsAbs can react with the CD3–TCR complex to initiate retargeted cytotoxicity without any MHC restriction [1,2]. In contrast, NK cells are a component of the body's innate immunity and can both lyse target cells and provide an early source of immunoregulatory cytokines [9]. Most human NK cells express high levels of FcγRIII (CD16), which plays a critical role in the induction of antibody-dependent cellular cytotoxicity (ADCC), which is one of the major modes of action of most therapeutic antibodies. Thus, CD16 is an attractive candidate for targeted immunotherapy, and effective CD16-mediated cytotoxicity induced by bispecific diabodies has been documented for malignant tumors [7,9].

Herein, we describe our construction of a second functional bispecific diabody against EGFR that uses an anti-CD16 variable fragment (Fv) to recruit a different subset of lymphocyte effectors, the NK cells. The resultant anti-EGFR × anti-CD16 bispecific diabody (Ex16) showed marked growth inhibitory activity that was clearly dependent on the effector cells. However, humanization of the diabody resulted in a considerable decrease in its growth inhibitory activity due to a reduction in its binding affinity. The Vernier zone [15], which is located near the complementarity-determining regions (CDRs), plays a role in the binding activity of antibodies. To recover the function of the diabody that had been lost as a result of its humanization, we introduced mutations in the Vernier zone residues by preparing 15 different humanized Ex16 (hEx16) mutants and selected the most functional one by using the *in vitro* refolding system described in an earlier report [13]. To our knowledge, this is the first report of a functional, fully humanized, bispecific diabody that can retarget EGFR and CD16 on tumor cells and was prepared with the use of our refolding system. Thus, our refolding system has again been demonstrated to be suitable for the efficient optimization of heterodimeric proteins.

Results

Preparation of refolded Ex16

To prepare Ex16 with specificity for EGFR and CD16, we applied the *in vitro* refolding system used for refolding of hEx3, as described previously [13,14]. The two chimeric single-chain components of Ex16, 3GHh5L and h5H3GL, were separately expressed in *Escherichia coli*. Results of SDS/PAGE and western blotting showed that each gene product was primarily and substantially present in the intracellular insoluble fractions (Fig. 1). Furthermore, high purity and stoichiometric association of chimeric single-chain components were observed in refolded Ex16 (Fig. 1), demonstrating the successful preparation of Ex16 using our *in vitro* refolding system.

Growth inhibitory effect of Ex16

To evaluate the inhibition of cancer growth by Ex16, we performed an MTS (3-(4,5-dimethylthiazole-2-yl)-5-(3-carboxymethoxyphenyl)-2-(4-sulfophenyl)-2*H*-tetrazolium, inner salt) assay with TFK-1 human bile duct carcinoma cells by using T-LAK cells or lymphokine-activated killer cells with the NK cell phenotype (NK-LAK) as effector cells. Ex16 inhibited the growth of cancer cells only in the presence of NK-LAK cells (Fig. 2A). Flow cytometric analyses showed that induced NK-LAK cells consisted largely (about 70%) of CD16-positive lymphocytes, whereas T-LAK cells consisted largely of CD3-positive lymphocytes (Fig. 2B). The specific binding of Ex16 to NK-LAK (Ex16) cells was also confirmed by use of flow cytometry (data not shown). These results indicate that the anti-EGFR × anti-CD16 bispecific diabody can inhibit EGFR-positive cancer growth in an effector cell dependent manner.

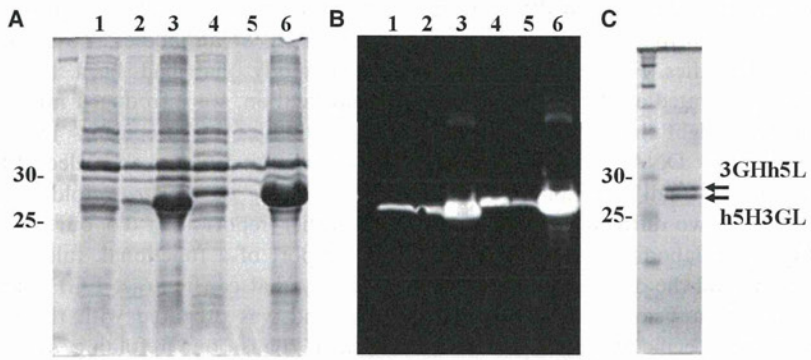

Fig. 1. Preparation of Ex16. (A), (C) SDS/PAGE under reducing conditions. (B) Western blot of *E. coli* BL21 (DE3) cells expressing 3GHh5L (lanes 1–3) and h5H3GL (lanes 4–6) using an anti-His-tag monoclonal antibody. Molecular size markers (in kilodaltons) are shown on the left in (B) and (C). In (A) and (B), lanes 1 and 4 represent proteins in the bacterial culture supernatant, lanes 2 and 5 represent proteins in the intracellular soluble fraction, and lanes 3 and 6 represent proteins in the intracellular insoluble fraction. C, refolded Ex16 diabody.

Humanization of Ex16 to reduce immunogenicity

Because Ex16 demonstrated anti-proliferative activity for cancer cells, we designed and prepared a fully humanized Ex16 (hEx16) to reduce the immunogenicity of Ex16 and make it more suitable for clinical use. The anti-EGFR Fvs used for the construction of Ex16 were already humanized [13], and we humanized the anti-CD16 Fvs from 3G8 by using the CDR-grafting method, as described in Materials and methods. We selected human sequences as templates for humanized 3G8 Fvs by doing homology searches, taking into account the lengths of the CDRs as well as the residues located at the VH–VL interface [16] and in the Vernier zone [15]. The sequences of the humanized 3G8 Fvs, shown in Fig. 3, were used to construct the hEx16 expression vectors pRA-h3GHh5L and pRA-h5Hh3GL. hEx16 was successfully prepared by using these vectors, and was subjected to *in vitro* refolding. However, a substantial decrease was seen in the growth inhibition by hEx16 in the MTS assay with the TFK-1 (Fig. 4A) and A431 (Fig. 4B) cell lines, both of which express high levels of EGFR. Decreased binding affinity due to the humanization of Ex16 may have resulted in the substantially lower growth inhibitory effects of hEx16.

Introduction of mutations into the Vernier zone of humanized 3G8 Fv in hEx16

All residues located at the VH–VL interface whose mutation would affect their interactions with the ligand were conserved in humanized *3G8*. However, two residues in each of the Vernier zones of VL and VH were mutated: M4L and G64A in VL, and S29R and R94Q in VH (Fig. 3). When affinity for the ligand is lost after humanization, as seen in the present case, the changed residues often need to be changed back into the corresponding residues in the original murine sequences. However, it is difficult to identify which residues or combinations of residues will critically contribute to the restoration of binding affinity. Therefore, we constructed resubstitution mutants in every possible combination, including single mutations, yielding 15 different hEx16 mutants (Table 1). All mutants were prepared similarly, were of high purity and underwent stoichiometric association of their chimeric single-chain components by using the *in vitro* refolding procedure described in Materials and methods (data not shown).

Binding and cancer growth inhibition by hEx16 mutants

Flow cytometric analysis and the MTS assay were performed to evaluate the binding and cancer growth inhibition by hEx16 mutants. Because induced NK-LAK cells contain some CD16-negative cells (Fig. 2B), we established a Chinese hamster ovary (CHO) cell line that stably expressed high levels of CD16 (CD16/CHO) to evaluate more clearly the differences in CD16-dependent binding of the bispecific diabodies. Comparable binding to EGFR-positive TFK-1 cells was observed for Ex16 and hEx16, and each mutant showed a slight increase in binding strength over hEx16 (Table 1). In contrast, the binding strength of hEx16 to CD16/CHO cells was much lower than that of Ex16, and some mutants showed a recovery of binding strength to over 10 times the original strength of hEx16 (Table 1). The cancer cell growth inhibition was also restored for several mutants (Fig. 5). Thus, the function of hEx16 could be restored by changing the residues in the Vernier zones back

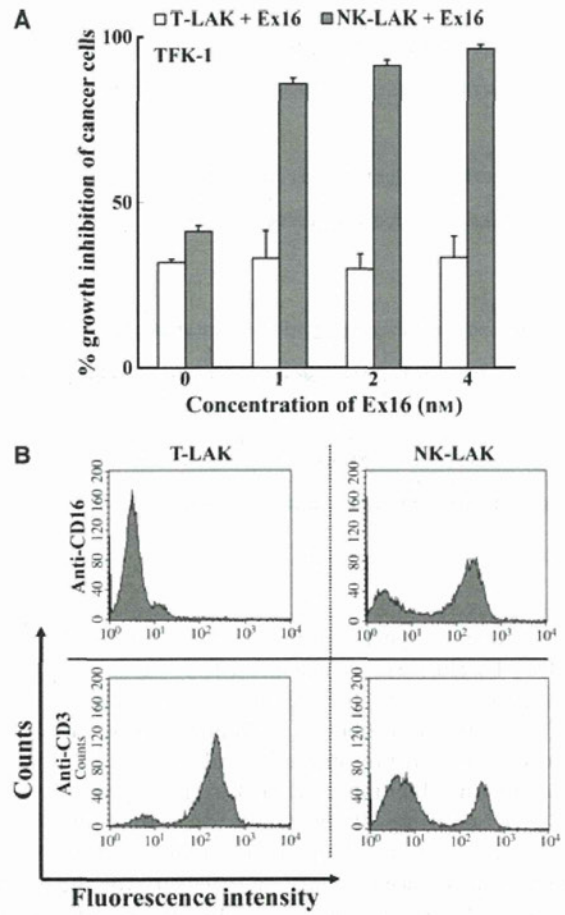

Fig. 2. Effector cell specificity and growth inhibition activity of Ex16. (A) Growth inhibition of EGFR-positive TFK-1 cells by Ex16 diabodies. Ex16 diabodies and T-LAK or NK-LAK effector cells were added to TFK-1 tumor cells at a ratio of 5 to 1 for T-LAK cells or 2.5 to 1 for NK-LAK cells. Data are presented as the mean values ± SD and are representative of at least three independent experiments with similar results. (B) Flow cytometric analysis of each type of effector cell. T-LAK cells and NK-LAK cells were incubated with either a mouse anti-CD16 antibody (3G8 IgG) or a mouse anti-CD3 antibody (OKT3 IgG), followed by an FITC-conjugated anti-mouse IgG.

into the ones present in the original murine sequences of Ex16.

Surface plasmon resonance analysis of fractionated dimers of an hEx16 mutant selected on the basis of its growth inhibitory effect

For further analyses, we limited our studies to certain mutants based on the results of flow cytometry and the MTS assay. Comparable growth inhibitory effects were observed between Mu 1 and 2, Mu 3 and 4, and Mu 11 and 12, respectively, in the MTS assay with TFK-1 cells (Fig. 5). We selected for further analyses those mutants that had fewer mouse sequences, i.e. Mu 1, Mu 3 and Mu 11, as some restoration in their binding strength for CD16 was also seen in flow cytometric analyses (Table 1). Gel filtration of each diabody showed the formation of 58-kDa dimers, but peaks corresponding to monomers and multimers were also observed (data for Ex16, hEx16 and Mu 3 are shown in Fig. 6A as representative examples). Fractionated Mu 3 diabodies (dimer fractions of ~ 58 kDa) showed the highest growth inhibition among all the selected mutants at any concentration in the MTS assay (Fig. 6B). Therefore, we compared the binding kinetics of Ex16, hEx16 and Mu 3 for CD16 by surface plasmon resonance (SPR) using fractionated diabodies. Marked decreases in both the association and dissociation rates were observed for hEx16, resulting in an affinity constant that was only 4% of the affinity constant for Ex16 (Table 2). In contrast, the binding kinetics of Mu 3 were comparable with those of Ex16 (Table 2), which probably contributed to the restoration of its cancer growth inhibition to a level comparable with that of Ex16.

Comparison of the growth inhibitory effect of Ex16, hEx16 and cetuximab

To compare the growth inhibitory effect of fractionated dimers of Ex16 and the most functional hEx16 mutant, Mu 3, with the US Food and Drug Administration approved therapeutic anti-EGFR antibody cetuximab, we performed the MTS assay with TFK-1 and A431 cells and peripheral blood mononuclear cells (PBMCs) as effector cells. Comparable growth inhibitory effects were observed for Ex16 and cetuximab in both cancer cell lines (Fig. 7A,B). Mu 3 also showed a growth inhibitory effect comparable with that of cetuximab, especially at high doses, thus demonstrating the successful construction of a fully humanized, CD16-targeted bispecific diabody with the potential to be a novel therapeutic antibody fragment.

Discussion

EGFR is overexpressed in a wide range of human malignancies, and its expression level is correlated with poor clinical outcome in patients with any of several cancers [17]. Therapeutically potent BsAbs targeting EGFR have been prepared by fusion of two hybridomas and by chemical conjugation; however, such classical methods have led to the formation of several nonfunctional analogs [18,19]. We previously reported

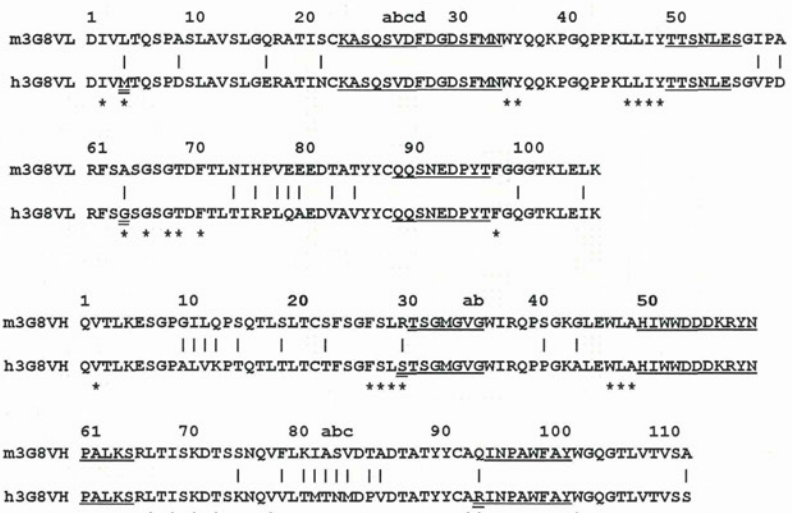

Fig. 3. Amino acid sequences of m3G8Fv and h3G8Fv. The numbering of residues and the definition of CDRs (underlined) were based on the work of Kabat *et al.* [45]. Differences in sequence are indicated by vertical lines, and framework positions characterized as Vernier zone residues are marked with asterisks [15]. Four mutation sites are double-underlined.

significant *in vitro* and *in vivo* antitumor activity of a humanized bispecific diabody that recruited T cells towards an EGFR-positive tumor (hEx3) [13]. Although studies to examine the usefulness of hEx3 for clinical therapy are currently under way, the most advanced BsAb fragment recruiting T cells, Micromet's blinatumomab, has shown promising results in a clinical study. However, it has also shown central nervous system symptoms, which have led to permanent discontinuation of the study drug in some cases [20]. Thus, in the present study, we tried to construct a second, functional, fully humanized, anti-EGFR diabody that would recruit another subset of lymphocyte effectors, the NK cells, to EGFR-expressing tumors.

To confirm the usefulness of an anti-EGFR × anti-CD16 diabody, we first prepared Ex16, which consists of a previously humanized, anti-EGFR 528 Fv and a mouse anti-CD16 3G8 Fv. Although downsizing antibodies enables their large-scale preparation by using bacterial expression systems, efficient preparation of functional small antibody fragments has often been hampered by the formation of insoluble aggregates in the cytoplasmic or periplasmic space [21]. We had previously developed an *in vitro* refolding system to prepare functional, bispecific diabodies from insoluble intracellular aggregates in *E. coli* [12,14], and we applied it in this study to the preparation of Ex16. We observed both a stoichiometric association of chimeric single-chain components and effector cell dependent growth inhibition with refolded Ex16 (Figs 1, 2), demonstrating the successful preparation of Ex16 with our *in vitro* refolding system and the usefulness of Ex16 for inhibiting the growth of cancer cells.

We then designed a humanized version of the anti-CD16 Fv (Fig. 3) to construct a fully humanized Ex16 (hEx16) in order to reduce the immune response against murine antibodies in human hosts. However, the resultant hEx16 showed a substantial decrease in the growth inhibition of EGFR-expressing cancer cells (Fig. 4). Grafting of the CDRs of murine antibodies onto appropriate human frameworks has often resulted in reduced affinity or specificity for the target antigen [22,23]. Because the CDR-grafting method is widely used for humanizing murine antibodies, there are a few general strategies for the recovery of the binding affinity of humanized antibodies, although these strategies often require several trial-and-error approaches [24–26]. The humanized Ex16 had reduced binding strength (Table 2); hence, we constructed hEx16 mutants to restore the ability of the diabody to inhibit the growth of EGFR-expressing cancer cells.

Previous work has suggested that residues in the β-sheet framework underlying the CDRs play a critical role in the adjustment of the loop structures of the CDRs; these residues are referred to as the Vernier zone [15]. Although residues located at the VH–VL interface have also been reported to be important [27], we focused only on the Vernier zone because the residues at the VH–VL interface were all conserved in humanized 3G8. Within the Vernier zone, two residues in VL and two in VH were mutated as a result of humanization. Because it is difficult to identify or predict which residue or combinations of residues can critically contribute to the recovery of binding affinity, we constructed mutants in every combination (i.e. 15 different hEx16 mutants).

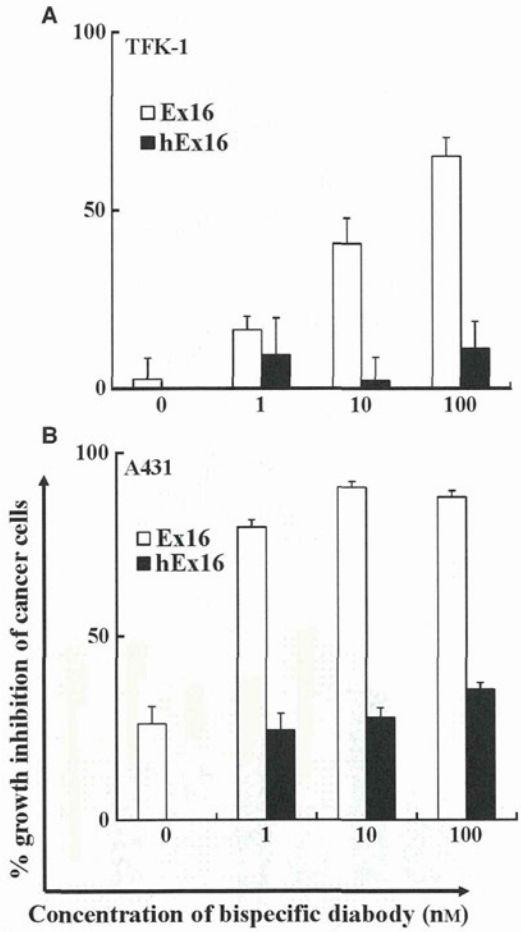

Fig. 4. Growth inhibition of EGFR-positive cell lines by Ex16 and hEx16. NK-LAK cells were added to TFK-1 cells (A) or A431 cells (B) at a ratio of 2.5 to 1. The results at concentrations of 0 nM show the spontaneous growth inhibition rate of the effector cells. Data are presented as the mean values ± SD and are representative of at least three independent experiments with similar results.

Table 1. Mutants constructed in this study and mean fluorescence intensity in flow cytometry. N.C., cells were incubated with $NaCl/P_i$.

	h5Hh3GL		h3GHh5H		Mean fluorescence intensity	
Mutants/ samples	M4L	G64A	S29R	R94Q	TFK-1 ($EGFR^+$)	CD16/ CHO
N.C.					7	5
Ex16					67	1476
hEx16					67	28
Mu 1	+				79	413
Mu 2	+		+		125	49
Mu 3	+			+	86	225
Mu 4	+		+	+	94	249
Mu 5		+			85	13
Mu 6		+	+		135	11
Mu 7		+		+	87	41
Mu 8		+	+	+	108	44
Mu 9	+	+			82	316
Mu 10	+	+	+		98	28
Mu 11	+	+		+	91	230
Mu 12	+	+	+	+	96	237
Mu 13			+		131	59
Mu 14				+	78	58
Mu 15			+	+	92	55

Bispecific diabodies are usually prepared using coexpression vectors containing two chimeric single-chain components from the culture supernatant or the periplasmic fraction [8,28]. In the present study, we would have needed to construct 15 different expression vectors if we had used a coexpression vector system. Instead, we were able to do this efficiently by combining four kinds of h5Hh3GL and h3GHh5H (Table 1). The most functional hEx16 mutant, Mu 3, demonstrated binding affinity comparable with Ex16 in SPR studies (Table 2) and a growth inhibitory effect comparable with that of cetuximab (Fig. 7). Thus, this method of separately expressing each chimeric single-chain component and refolding the two chimeric single-chain components after stoichiometric mixing could be used to efficiently prepare diabody mutants, especially when many mutants need to be constructed. All BsAb fragments currently in clinical trials, such as blinatumomab [29] and Affimed's AFM13 (http://www.affimed.com/afm13), are produced in expensive mammalian expression systems even though they are small-format antibody derivatives. Our *in vitro* refolding system could provide a low-cost alternative production method based on a bacterial expression system for similar BsAb products.

The values of affinity (148 nM) and EC50 (1.2 nM calculated for A431) for hEx16 are lower than those previously reported for BsAb fragments based on anti-CD16 Fv [30–32], and a more homogeneous preparation is desired. To date, several different small BsAb fragments have been proposed to increase efficacy; in the cases of BsAb fragments targeting CD16, the formats designed with two binding sites for tumor cells especially have shown remarkably low EC values [31,32]. However, they are also produced in mammalian expression systems, like the advanced BsAb fragments described above. A previous report [28] and our unpublished data showed that the orientation of the variable domains of the diabody can influence the expression and formation of active binding sites. Thus, we are working to further improve hEx16 by converting

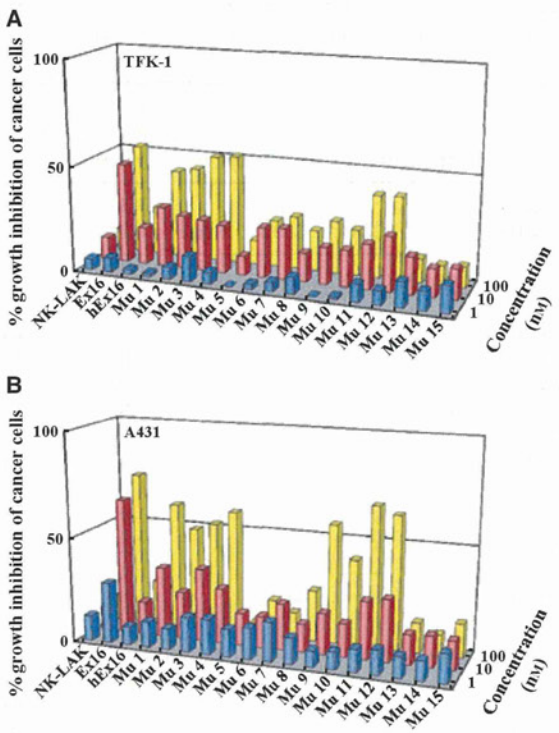

Fig. 5. Growth inhibition of EGFR-positive cell lines by Ex16, hEx16 and mutant hEx16 diabodies. NK-LAK cells were added to TFK-1 cells (A) or A431 cells (B) at a ratio of 2.5 to 1. Data are presented as the mean values ± SD and are representative of at least three independent experiments with similar results.

the orientation of the variable domains and to optimize its homogeneous preparation by creating additional mutations.

In conclusion, we efficiently constructed a humanized anti-EGFR × anti-CD16 diabody with a growth inhibitory effect comparable with that of cetuximab by using a proven *in vitro* refolding method. Our refolding system may allow industrial-scale production of bispecific diabodies and also aid in the efficient optimization of additional proteins with heterodimeric structures.

Materials and methods

Preparation of Ex16 diabodies

The mouse hybridoma cell line 3G8 was used as the source of the anti-human CD16 variable region genes. The *VH* and *VL* genes of the anti-human CD16 Fv were cloned with primers synthesized based on the sequences of genes described in an earlier report [33] and designated *3GH* and *3GL*, respectively. We previously reported the construction of the bacterial expression vectors pRA-hOHh5L and pRA-

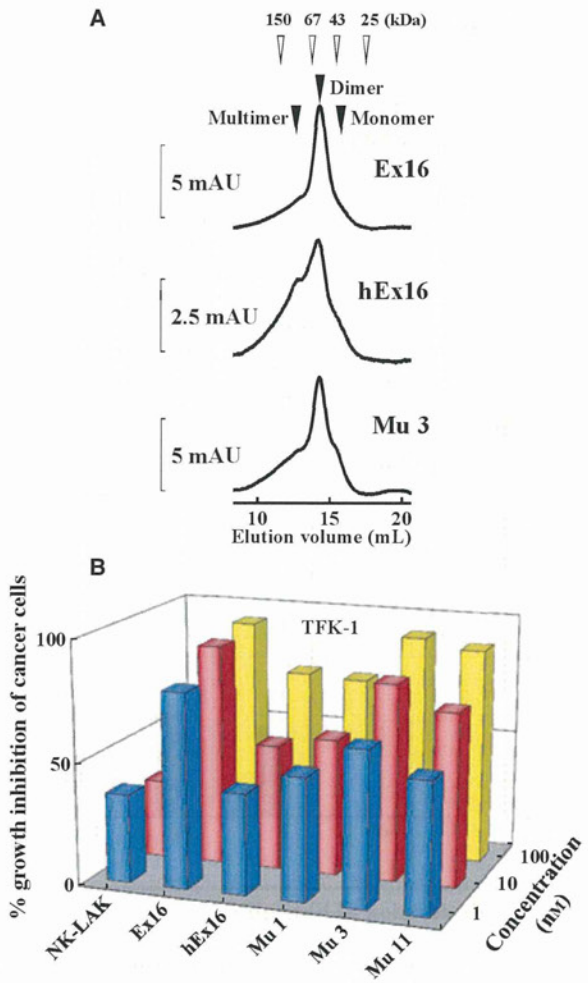

Fig. 6. Growth inhibition of EGFR-positive TFK-1 by fractionated diabodies. (A) Gel filtration of refolded diabodies; mAU, milliabsorbance unit. (B) NK-LAK cells were added to TFK-1 cells at a ratio of 2.5 to 1. Data are presented as the mean values ± SD and are representative of at least three independent experiments with similar results.

h5HhOL, which were designed to express the two chimeric single-chain components h5HhOL and hOHh5L, respectively, of a humanized anti-EGFR × anti-CD3 bispecific diabody (hEx3) [13]. The genes coding for the VH and VL regions of the humanized anti-CD3 antibody OKT3 Fv, *hOH* and *hOL* respectively, were replaced with *3GH* and *3GL*, which code for the VH and VL regions of the anti-human CD16 Fv. The resulting vectors, pRA-3GHh5L and pRA-h5H3GL, were used to prepare Ex16 using the *in vitro* refolding system described in our earlier report [13]. Briefly, 3GHh5L and h5H3GL chimeric single-chain components were individually purified through a TALON Metal Affinity Resin column (Clontech, Palo Alto, CA, USA) from the intracellular insoluble fraction after solubilization with 6 M guanidinium hydrochloride/phosphate-buffered

Table 2. K_D values for CD16 evaluated by using surface plasmon resonance.

	k_{on} ('10^4 $M^{-1}\cdot s^{-1}$)	k_{off} ('$10^{-2}\cdot s^{-1}$)	K_D ('10^{-9} M)
3G8 IgG	7.9	0.078	9.9
3G8 Fab	23.8	1.7	71
Ex16	12.2	2.5	203
hEx16	0.2	0.8	4300
Mu 3	13.3	2.0	148

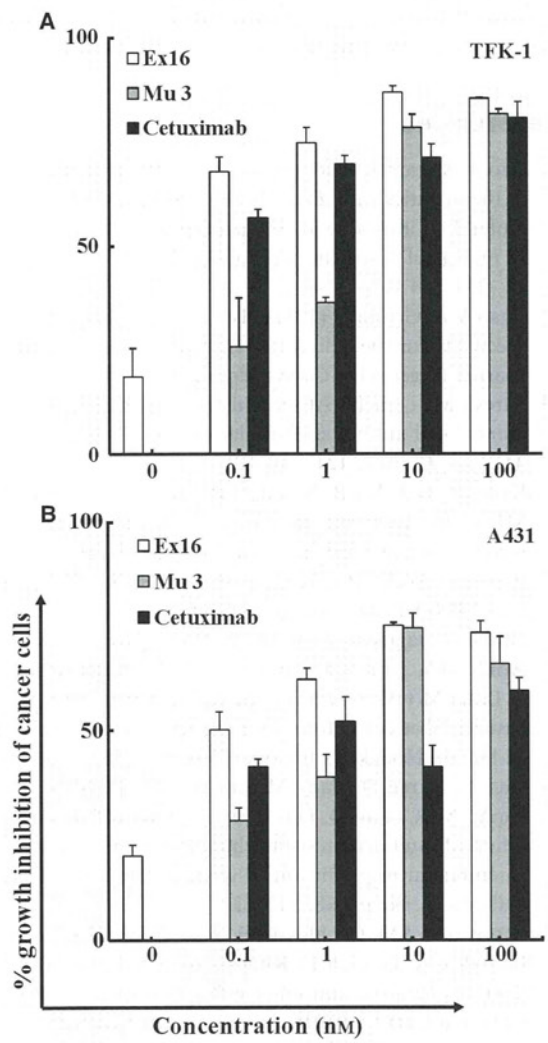

Fig. 7. Growth inhibition of EGFR-positive cell lines by Ex16, Mu 3 and cetuximab. Antibodies and PBMCs were added to TFK-1 cells or A431 cells at a ratio of 20 to 1. The results at concentrations of 0 nM show the spontaneous growth inhibition rate of the effector cells. Data are presented as the mean values ± SD and are representative of at least three independent experiments with similar results.

saline (Gu-HCl/NaCl/P_i). Each of the chimeric single-chain component solutions was diluted to 15 μM with 6 M Gu-HCl/NaCl/P_i, and the resulting solutions were then mixed in a 1 : 1 ratio. The denatured chimeric single-chain component mixture (5 mL) underwent stepwise dialysis into NaCl/P_i through solutions of 3, 2, 1 and 0.5 M Gu-HCl/NaCl/P_i.

Preparation of effector cells

T-LAK cells were induced as previously reported [34]. Briefly, PBMCs were cultured for 48 h at a density of 1×10^6 cells·mL^{-1} in a growth medium supplemented with 100 IU·mL^{-1} of recombinant human interleukin-2 (kindly supplied by Shionogi Pharmaceutical Co., Osaka, Japan). The culture flask (A/S Nunc, Roskilde, Denmark) containing the T-LAK cells had been precoated with an anti-CD3 mAb (10 μg·mL^{-1}). For the induction of NK-LAK cells, PBMCs were co-cultured for 48 h at a density of 1×10^6 cells·mL^{-1} with MUC1/B7-cotransfected K562 cells (an irradiated cancer vaccine cell line) at a density of 2×10^5 cells·mL^{-1} in a growth medium supplemented with 200 IU·mL^{-1} of recombinant human interleukin-2 and 1% human plasma.

Flow cytometric analyses

CHO cells were transfected with the CD16 expression vector pcDNA-CD16 by using Lipofectamine 2000 (Invitrogen, Groningen, The Netherlands) for the establishment of a CHO clone that stably expressed CD16 (CD16/CHO). Test CD16/CHO cells (1×10^6) were incubated on ice with 200 pmol of bispecific diabodies for 30 min. The incubated cells were washed with NaCl/P_i containing 0.1% NaN_3 and were then incubated for 30 min on ice with a fluorescein isothiocyanate (FITC) conjugated secondary antibody with an affinity for the c-myc tag (9E10; Santa Cruz Biotechnology, Santa Cruz, CA, USA). The FITC-labeled cells were subsequently analyzed by use of flow cytometry (FACSCalibur; Becton Dickinson, San Jose, CA, USA) [35].

In vitro growth inhibition assay

In vitro growth inhibition of TFK-1 (human bile duct carcinoma) cells and A431 (human epidermoid cancer) cells was assayed with an MTS assay kit (CellTiter 96 AQueous Non-Radioactive Cell Proliferation Assay; Promega, Madison, WI, USA), as reported previously [36]. Half-maximal effective concentration (EC50) values were calculated by using a sigmoidal dose–response curve fit.

Construction and preparation of hEx16 diabodies

An anti-CD16 Fv was humanized by using CDR-grafting methods, as described previously [37–39]. Based on

homology searches with human antibodies using the BLAST sequence program, the sequence of sc77u-41 VH [NCBI protein database (http://www.ncbi.nlm.nih.gov/protein); accession no. AAD53863] [40] was chosen as the template for 3G8 VH, and the sequence of Hod VL (accession no. AAD03723) [41] was chosen as the template for 3G8 VL. VH and VL sequences containing the CDRs were designed by substituting the 3G8 CDRs with the chosen sequences and were then constructed by using PCR overlap methods and synthesized primers that had been optimized for *E. coli*. The resulting genes were designated *h3GH* and *h3GL* and were used to replace *3GH* and *3GL* in the pRA-3GHh5L and pRA-h5H3GL to create the constructs pRA-h3GHh5L and pRA-h5Hh3GL, respectively, as described above. The hEx16 diabodies were prepared using the aforementioned bacterial expression and *in vitro* refolding systems.

Construction and preparation of hEx16 mutants

Site-directed mutagenesis was performed as described previously [42]. Three kinds of mutants were constructed for each of the h3GHh5L and h5Hh3GL chimeric single-chain components. For the preparation of hEx16 mutants, eight chimeric single-chain components, including two wild-type chimeric single-chain components, were prepared individually. The denatured h3GHh5Ls and h5Hh3GLs were then mixed stoichiometrically in every possible combination and subsequently refolded. The hEx16 mutants constructed in this study are summarized in Table 1.

Gel filtration chromatography

Gel filtration analysis was done with a Hiload Superdex 200-pg column (10/300; GE Healthcare Bio-Science Corp., Piscataway, NJ, USA) to fractionate the dimers of each bispecific diabody. The column was equilibrated with NaCl/P_i and then 0.25 mL of purified bispecific diabodies were loaded onto the column at a flow rate of 0.5 mL·min^{-1}.

Surface plasmon resonance

The interactions between CD16 and IgG or antibody fragments were analyzed by using SPR spectroscopy with Biacore 2000 (GE Healthcare). CD16 was prepared in accordance with the method in a previous report [43] and immobilized onto the cells in a CM5 sensor chip to achieve levels of up to 3183 resonance units. Solutions of various concentrations of IgG or antibody fragments in 0.005% NaCl/P_i–Tween 20 were passed over the immobilized CD16. The data were normalized by subtracting the response of a blank cell after blocking. BIAEVALUATION software (GE Healthcare) was used to analyze the data. Kinetics parameters were calculated by using a global fitting analysis with the assumptions of the 1 : 1 Langmuir binding model [44].

Acknowledgements

This work was supported by Grants-in-Aid for Scientific Research from the Ministry of Education, Science, Sports, and Culture of Japan (R.A. and I.K.) and by grants from the New Energy and Industrial Technology Development Organization of Japan. Additional support was provided through the Program for Promotion of Fundamental Studies in Health Sciences of the National Institute of Biomedical Innovation.

References

1 Cao Y & Lam L (2003) Bispecific antibody conjugates in therapeutics. *Adv Drug Del Rev* **55**, 171–197.
2 Kufer P, Lutterbuse R & Baeuerle PA (2004) A revival of bispecific antibodies. *Trends Biotechnol* **22**, 238–244.
3 Raso V & Griffin T (1981) Hybrid antibodies with dual specificity for the delivery of ricin to immunoglobulin-bearing target cells. *Cancer Res* **41**, 2073–2078.
4 Suresh MR, Cuello AC & Milstein C (1986) Bispecific monoclonal antibodies from hybrid hybridomas. *Methods Enzymol* **121**, 210–228.
5 Kriangkum J, Xu B, Nagata LP, Fulton RE & Suresh MR (2001) Bispecific and bifunctional single chain recombinant antibodies. *Biomol Eng* **18**, 31–40.
6 Perisic O, Webb PA, Holliger P, Winter G & Williams RL (1994) Crystal structure of a diabody, a bivalent antibody fragment. *Structure* **2**, 1217–1226.
7 Arndt MA, Krauss J, Kipriyanov SM, Pfreundschuh M & Little M (1999) A bispecific diabody that mediates natural killer cell cytotoxicity against xenotransplantated human Hodgkin's tumors. *Blood* **94**, 2562–2568.
8 Gao Y, Xiong D, Yang M, Liu H, Peng H, Shao X, Xu Y, Xu C, Fan D, Qin L *et al.* (2004) Efficient inhibition of multidrug-resistant human tumors with a recombinant bispecific anti-P-glycoprotein x anti-CD3 diabody. *Leukemia* **18**, 513–520.
9 Kipriyanov SM, Cochlovius B, Schafer HJ, Moldenhauer G, Bahre A, Le Gall F, Knackmuss S & Little M (2002) Synergistic antitumor effect of bispecific CD19 x CD3 and CD19 x CD16 diabodies in a preclinical model of non-Hodgkin's lymphoma. *J Immunol* **169**, 137–144.
10 Xiong D, Xu Y, Liu H, Peng H, Shao X, Lai Z, Fan D, Yang M, Han J, Xie Y *et al.* (2002) Efficient inhibition of human B-cell lymphoma xenografts with an anti-CD20 x anti-CD3 bispecific diabody. *Cancer Lett* **177**, 29–39.

11 Asano R, Takemura S, Tsumoto K, Sakurai N, Teramae A, Ebara S, Katayose Y, Shinoda M, Suzuki M, Imai K *et al.* (2000) Functional construction of the anti-mucin core protein (MUC1) antibody MUSE11 variable regions in a bacterial expression system. *J Biochem (Tokyo)* **127**, 673–679.
12 Asano R, Kudo T, Nishimura Y, Makabe K, Hayashi H, Suzuki M, Tsumoto K & Kumagai I (2002) Efficient construction of a diabody using a refolding system: anti-carcinoembryonic antigen recombinant antibody fragment. *J Biochem (Tokyo)* **132**, 903–909.
13 Asano R, Sone Y, Makabe K, Tsumoto K, Hayashi H, Katayose Y, Unno M, Kudo T & Kumagai I (2006) Humanization of the bispecific epidermal growth factor receptor x CD3 diabody and its efficacy as a potential clinical reagent. *Clin Cancer Res* **12**, 4036–4042.
14 Asano R, Sone Y, Ikoma K, Hayashi H, Nakanishi T, Umetsu M, Katayose Y, Unno M, Kudo T & Kumagai I (2008) Preferential heterodimerization of a bispecific diabody based on a humanized anti-EGFR antibody 528. *Protein Eng Des Sel* **21**, 597–603.
15 Foote J & Winter G (1992) Antibody framework residues affecting the conformation of the hypervariable loops. *J Mol Biol* **224**, 487–499.
16 Vargas-Madrazo E & Paz-Garcia E (2003) An improved model of association for VH-VL immunoglobulin domains: asymmetries between VH and VL in the packing of some interface residues. *J Mol Recognit* **16**, 113–120.
17 Fischer-Colbrie J, Witt A, Heinzl H, Speiser P, Czerwenka K, Sevelda P & Zeillinger R (1997) EGFR and steroid receptors in ovarian carcinoma: comparison with prognostic parameters and outcome of patients. *Anticancer Res* **17**, 613–619.
18 Ferrini S, Cambiaggi A, Sforzini S, Marciano S, Canevari S, Mezzanzanica D, Colnaghi MI, Grossi CE & Moretta L (1993) Targeting of T lymphocytes against EGF-receptor+ tumor cells by bispecific monoclonal antibodies: requirement of CD3 molecule cross-linking for T-cell activation. *Int J Cancer* **55**, 931–937.
19 Pfosser A, Brandl M, Salih H, Grosse-Hovest L & Jung G (1999) Role of target antigen in bispecific-antibody-mediated killing of human glioblastoma cells: a pre-clinical study. *Int J Cancer* **80**, 612–616.
20 Nagorsen D & Baeuerle PA (2011) Immunomodulatory therapy of cancer with T cell-engaging BiTE antibody blinatumomab. *Exp Cell Res* **317**, 1255–1260.
21 Tsumoto K, Shinoki K, Kondo H, Uchikawa M, Juji T & Kumagai I (1998) Highly efficient recovery of functional single-chain Fv fragments from inclusion bodies overexpressed in *Escherichia coli* by controlled introduction of oxidizing reagent – application to a human single-chain Fv fragment. *J Immunol Methods* **219**, 119–129.
22 Jones PT, Dear PH, Foote J, Neuberger MS & Winter G (1986) Replacing the complementarity-determining regions in a human antibody with those from a mouse. *Nature* **321**, 522–525.
23 Riechmann L, Clark M, Waldmann H & Winter G (1988) Reshaping human antibodies for therapy. *Nature* **332**, 323–327.
24 Queen C, Schneider WP, Selick HE, Payne PW, Landolfi NF, Duncan JF, Avdalovic NM, Levitt M, Junghans RP & Waldmann TA (1989) A humanized antibody that binds to the interleukin 2 receptor. *Proc Natl Acad Sci U S A* **86**, 10029–10033.
25 Co MS, Deschamps M, Whitley RJ & Queen C (1991) Humanized antibodies for antiviral therapy. *Proc Natl Acad Sci U S A* **88**, 2869–2873.
26 Ohtomo T, Tsuchiya M, Sato K, Shimizu K, Moriuchi S, Miyao Y, Akimoto T, Akamatsu K, Hayakawa T & Ohsugi Y (1995) Humanization of mouse ONS-M21 antibody with the aid of hybrid variable regions. *Mol Immunol* **32**, 407–416.
27 Nakanishi T, Tsumoto K, Yokota A, Kondo H & Kumagai I (2008) Critical contribution of VH-VL interaction to reshaping of an antibody: the case of humanization of anti-lysozyme antibody, HyHEL-10. *Protein Sci* **17**, 261–270.
28 Lu D, Jimenez X, Witte L & Zhu Z (2004) The effect of variable domain orientation and arrangement on the antigen-binding activity of a recombinant human bispecific diabody. *Biochem Biophys Res Commun* **318**, 507–513.
29 Loffler A, Kufer P, Lutterbuse R, Zettl F, Daniel PT, Schwenkenbecher JM, Riethmuller G, Dorken B & Bargou RC (2000) A recombinant bispecific single-chain antibody, CD19 × CD3, induces rapid and high lymphoma-directed cytotoxicity by unstimulated T lymphocytes. *Blood* **95**, 2098–2103.
30 Bruenke J, Barbin K, Kunert S, Lang P, Pfeiffer M, Stieglmaier K, Niethammer D, Stockmeyer B, Peipp M, Repp R *et al.* (2005) Effective lysis of lymphoma cells with a stabilised bispecific single-chain Fv antibody against CD19 and FcgammaRIII (CD16). *Br J Haematol* **130**, 218–228.
31 Kellner C, Bruenke J, Stieglmaier J, Schwemmlein M, Schwenkert M, Singer H, Mentz K, Peipp M, Lang P, Oduncu F *et al.* (2008) A novel CD19-directed recombinant bispecific antibody derivative with enhanced immune effector functions for human leukemic cells. *J Immunother* **31**, 871–884.
32 Singer H, Kellner C, Lanig H, Aigner M, Stockmeyer B, Oduncu F, Schwemmlein M, Stein C, Mentz K, Mackensen A *et al.* (2010) Effective elimination of acute myeloid leukemic cells by recombinant bispecific antibody derivatives directed against CD33 and CD16. *J Immunother* **33**, 599–608.
33 Bruenke J, Fischer B, Barbin K, Schreiter K, Wachter Y, Mahr K, Titgemeyer F, Niederweis M, Peipp M, Zunino SJ *et al.* (2004) A recombinant bispecific

single-chain Fv antibody against HLA class II and FcgammaRIII (CD16) triggers effective lysis of lymphoma cells. *Br J Haematol* **125**, 167–179.
34 Asano R, Ikoma K, Kawaguchi H, Ishiyama Y, Nakanishi T, Umetsu M, Hayashi H, Katayose Y, Unno M, Kudo T *et al.* (2010) Application of the Fc fusion format to generate tag-free bi-specific diabodies. *FEBS J* **277**, 477–487.
35 Asano R, Kawaguchi H, Watanabe Y, Nakanishi T, Umetsu M, Hayashi H, Katayose Y, Unno M, Kudo T & Kumagai I (2008) Diabody-based recombinant formats of humanized IgG-like bispecific antibody with effective retargeting of lymphocytes to tumor cells. *J Immunother* **31**, 752–761.
36 Asano R, Ikoma K, Sone Y, Kawaguchi H, Taki S, Hayashi H, Nakanishi T, Umetsu M, Katayose Y, Unno M *et al.* (2010) Highly enhanced cytotoxicity of a dimeric bispecific diabody, the hEx3 tetrabody. *J Biol Chem* **285**, 20844–20849.
37 Ono K, Ohtomo T, Yoshida K, Yoshimura Y, Kawai S, Koishihara Y, Ozaki S, Kosaka M & Tsuchiya M (1999) The humanized anti-HM1.24 antibody effectively kills multiple myeloma cells by human effector cell-mediated cytotoxicity. *Mol Immunol* **36**, 387–395.
38 Sato K, Tsuchiya M, Saldanha J, Koishihara Y, Ohsugi Y, Kishimoto T & Bendig MM (1993) Reshaping a human antibody to inhibit the interleukin 6-dependent tumor cell growth. *Cancer Res* **53**, 851–856.
39 Sato K, Tsuchiya M, Saldanha J, Koishihara Y, Ohsugi Y, Kishimoto T & Bendig MM (1994) Humanization of a mouse anti-human interleukin-6 receptor antibody comparing two methods for selecting human framework regions. *Mol Immunol* **31**, 371–381.
40 Wang X & Stollar BD (1999) Immunoglobulin VH gene expression in human aging. *Clin Immunol* **93**, 132–142.
41 Ramsland PA, Brock CR, Moses J, Robinson BG, Edmundson AB & Raison RL (1999) Structural aspects of human IgM antibodies expressed in chronic B lymphocytic leukemia. *Immunotechnology* **4**, 217–229.
42 Yokota A, Tsumoto K, Shiroishi M, Kondo H & Kumagai I (2003) The role of hydrogen bonding via interfacial water molecules in antigen-antibody complexation. The HyHEL-10-HEL interaction. *J Biol Chem* **278**, 5410–5418.
43 Sondermann P & Jacob U (1999) Human Fcgamma receptor IIb expressed in *Escherichia coli* reveals IgG binding capability. *Biol Chem* **380**, 717–721.
44 Asano R, Ikoma K, Shimomura I, Taki S, Nakanishi T, Umetsu M & Kumagai I (2011) Cytotoxic enhancement of a bispecific diabody by format conversion to tandem single-chain variable fragment (taFv): the case of the hEx3 diabody. *J Biol Chem* **286**, 1812–1818.
45 Kabat EA, Wu TT, Perry HM, Gottesman KS & Foeller C (1991) *Sequences of Proteins of Immunological Interest*, 5th edn. National Institutes of Health, Bethesda, MD.

J Mater Sci: Mater Med (2012) 23:2399–2412
DOI 10.1007/s10856-012-4671-x

In vitro and in vivo investigations of upconversion and NIR emitting $Gd_2O_3:Er^{3+},Yb^{3+}$ nanostructures for biomedical applications

Eva Hemmer · Hiroyuki Takeshita · Tomoyoshi Yamano · Takanori Fujiki · Yvonne Kohl · Karin Löw · Nallusamy Venkatachalam · Hiroshi Hyodo · Hidehiro Kishimoto · Kohei Soga

Received: 31 October 2011 / Accepted: 2 May 2012 / Published online: 16 May 2012

Abstract The use of an "over 1000-nm near-infrared (NIR) in vivo fluorescence bioimaging" system based on lanthanide containing inorganic nanostructures emitting in the visible and NIR range under 980-nm excitation is proposed. It may overcome problems of currently used biomarkers including color fading, phototoxicity and scattering. $Gd_2O_3:Er^{3+},Yb^{3+}$ nanoparticles and nanorods showing upconversion and NIR emission are synthesized and their cytotoxic behavior is investigated by incubation with B-cell hybridomas and macrophages. Surface modification with PEG-*b*-PAAc provides the necessary chemical durability reducing the release of toxic Gd^{3+} ions. NIR fluorescence microscopy is used to investigate the suitability of the nanostructures as NIR–NIR biomarkers. The in vitro uptake of bare and modified nanostructures by macrophages is investigated by confocal laser scanning microscopy. In vivo investigations revealed nanostructures in liver, lung, kidneys and spleen a few hours after injection into mice, while most of the nanostructures have been removed from the body after 24 h.

Electronic supplementary material The online version of this article (doi:10.1007/s10856-012-4671-x) contains supplementary material, which is available to authorized users.

E. Hemmer (✉) · H. Hyodo · H. Kishimoto · K. Soga
Center for Technologies Against Cancer (CTC), Tokyo University of Science, 2669 Yamazaki, Chiba 278-0022, Japan
e-mail: eva.hemmer@sogalabo.jp

H. Takeshita · T. Yamano · H. Kishimoto
Division of Immunobiology, Research Institute for Biological Sciences, Tokyo University of Science, 2669 Yamazaki, Chiba 278-0022, Japan

T. Fujiki · N. Venkatachalam · H. Hyodo · K. Soga
Department of Materials Science and Technology, Tokyo University of Science, 2641 Yamazaki, Chiba 278-8510, Japan

Y. Kohl · K. Löw
Department of Cell Biology & Applied Virology, Fraunhofer Institute for Biomedical Engineering, Ensheimer Straße 48, 66386 St. Ingbert, Germany

1 Introduction

Biocompatible nanomaterials have become the focus of intensive research due to their manifold applications ranging from implants and scaffolds [1–3], drug delivery and controlled release [4–9] to cell-tracking and bioimaging [10, 11]. Bioimaging is an important tool to visualize and investigate biological phenomena and in diagnostics. The early and reliable detection of diseases such as cancer, heart or neural diseases is essential for successful treatment and much effort has been undertaken in the field of nanomedicine [12–14]. Commonly, organic dyes and fluorescent proteins are used as fluorescent markers [15, 16]. Recently, semiconductor quantum dots (e.g. CdSe) have been proposed as biomarkers due to their tunable optical properties [17]. However, organic dyes suffer from color fading restricting their temporal use [15, 18], auto-fluorescence of the biological tissue and phototoxicity as well as scattering when ultraviolet (UV) light is used as excitation source. The main disadvantages of semiconductor quantum dots are their intrinsic toxicity requiring core–shell structures, such as CdTe/ZrO_2 or CdSe/CdS, and the blinking of their luminescence emission [19–21]. Due to their outstanding optical properties, such as sharp emission lines, long lifetimes and photostability, lanthanide (Ln) containing compounds may overcome those drawbacks [22]. In addition to their luminescence behavior, their magnetic properties make Ln-containing compounds promising candidates for bioimaging applications as hybrid

(opto-magneto) biomarkers [23, 24]. Luminescent rare earth doped gadolinium oxide nanorods exhibiting good T1-weighted MRI contrast have been reported by Tan et al. [25]. Alkaline-earth metal fluoride nanocrystals doped with Gd^{3+} have been proposed by Pang et al. as bifunctional biomarkers due to their magnetism and luminescence [26]. Ceramic host materials doped with erbium ions are known as upconverting (UPC) phosphors that absorb near-infrared (NIR) radiation and emit in the visible spectrum. Synthesis of poly(ethylene glycol)/streptavidin coimmobilized upconverting Y_2O_3:Er^{3+},Yb^{3+} nanophosphors and their potential as biomarkers have been reported by our own group [27]. Xiong et al. [28] described peptide-labeled $NaYF_4$: 20%Yb, 1.8%Er, 0.2%Tm nanophosphors for the in vivo imaging of tumors. Herein, main advantages of NIR light are the reduced phototoxicity, autofluorescence and scattering when compared to UV light. Reduced scattering allows a deeper penetration depth into biological tissue due to its NIR transparency also known as biological window [29]. However, the use of NIR to visible upconverting biomarkers still suffers from the reduced penetration depth and scattering of the emitted visible light. Therefore, NIR absorbing and NIR emitting inorganic materials as well as organic compounds are attracting increasing attention and are expected to be suitable nanoprobes for in vivo bioimaging. Hilderbrand et al. [30] reported the successful application of Y_2O_3 nanoparticles modified with NIR emitting fluorophores as NIR–NIR biomarkers. Prasad et al. [31] reported in vivo bioimaging of whole-body animal by use of Tm^{3+}/Yb^{3+} co-doped $NaYF_4$. Further, Gd^{3+} and Er^{3+}/Yb^{3+}/Eu^{3+} doped $NaYF_4$ and Tm^{3+}/Er^{3+}/Yb^{3+} co-doped $NaGdF_4$ nanocrystals have been suggested as bifunctional bioprobes due to their NIR–NIR emission and magnetic resonance properties [32–34]. With regards to clinical application NIR–NIR biomarkers are suitable image-guidance tools in surface-near (millimeter range) surgery as shown by Frangioni et al. [35, 36]. Using a fluorescence microscope equipped with an InGaAs-CCD liposome-encapsulated Y_2O_3:Er^{3+} nanostructures emitting NIR fluorescence at 1,550 nm under 980-nm excitation have been investigated for in vitro analysis by Soga et al. [37]. For further evaluation of the potential of biomarkers based on Ln-ions, which efficiently emit in the over-1000-nm NIR range, an "over-1000-nm NIR in vivo fluorescence bioimaging" (OTN-NIR-IFBI) system consisting of a 980-nm laser diode with a scanner for the fluorescence excitation and an InGaAs-CCD, which can detect the image in between 800 and 1,700 nm, was developed by our group. NIR fluorescence microscopy is used for in vitro cellular imaging on a micron scale level. In contrast, the new OTN-NIR-IFBI system allows not only in vitro but also in vivo imaging on a micron to millimeter scale including investigations of, e.g. uptake of nanostructures by organs, their in vivo distribution or their suitability as new markers in cell tracking.

Previously, we reported the preparation of bare and poly(ethylene glycol)-*b*-poly(acrylic acid) (PEG-*b*-PAAc) modified Gd_2O_3:Er^{3+},Yb^{3+} nanostructures and the investigation of their in vitro cytotoxicity by incubation with B-cell hybridomas and macrophages [38]. While no cytotoxic effect was observed towards B-cell hybridomas, bare nanostructures induced a toxic effect on macrophages. This observation was deduced to the poor chemical durability of Gd_2O_3 and formation of toxic Gd^{3+} when the nanostructures are uptaken by macrophages. Surface modification with PEG-*b*-PAAc provided the necessary chemical durability resulting in good in vitro biocompatibility. In the present study, the effect of PEG-*b*-PAAc modification on the in vitro cellular up-take of gadolinium oxide nanostructures by macrophages was investigated by confocal laser scanning microscopy (CLSM) using the upconversion emission of Gd_2O_3:Er^{3+},Yb^{3+} under 980-nm excitation. Further, the in vivo distribution of PEG-*b*-PAAc modified Gd_2O_3:Er^{3+},Yb^{3+} nanorods by hydrothermal synthesis (l/d $\sim$ 5) and nanoparticles (d $\sim$ 85–210 nm) by homogeneous precipitation (HP) method was evaluated. Herein, the imaging was performed by using the lately developed "1000-nm NIR in vivo fluorescence bioimaging" (OTN-NIR-IFBI) system.

2 Materials and methods

2.1 Material synthesis

Starting materials like lanthanide nitrates [Ln = Gd (min. 99.95 %, Kanto Chemical Co., Inc., Tokyo, Japan), Er (>99 %, Kojundo Kagaku Kenkyusho Co., Japan), Yb (99.9 %, Kojundo Kagaku Kenkyusho Co., Japan)], urea (min. 99.0 %, Kanto Chemical Co., Inc., Tokyo, Japan), PEG-6.000 [poly(ethylene glycol), Mw = 6,000, Kanto Chemical Co., Inc., Tokyo, Japan], cetyltrimethylammonium bromide (CTAB, Wako Pure Chemical Industries, Ltd., Osaka, Japan), ammonia (25 % aqueous solution, Kanto Chemical Co., Inc., Tokyo, Japan), and poly(ethylene glycol)-*b*-poly(acrylic acid) [PEG-*b*-PAAc block copolymer, Mw = 5,000/3,200, Polymersource, Dorval (Montreal), Canada] were used without further purification.

For HP, 1.68 mmol $Gd(NO_3)_3{\cdot}6H_2O$, 1 mol% $Er(NO_3)_3{\cdot}5H_2O$ and 1 mol% $Yb(NO_3)_3{\cdot}xH_2O$ were dissolved in 300 mL H_2O. As surfactant either 1–10 mmol CTAB or 1–10 mmol CTAB and 5 mmol PEG-6.000 were added, followed by stirring for 50 min at room temperature. 150 mmol urea were added to the pure Ln- or Ln-surfactant-solution and the mixture was kept stirring for 10 min. For precipitation, the mixture was stirred at 85 °C

for 30 min. In hydrothermal synthesis (HT), the concentration of gadolinium nitrate was set to 0.05 mol/L at a total volume of 30 mL. Therefore, 1.5 mmol $Gd(NO_3)_3{\cdot}6H_2O$ and an appropriate amount of $Er(NO_3)_3{\cdot}5H_2O$ and $Yb(NO_3)_3{\cdot}xH_2O$ (each 1 mol%) were dissolved in 9 mL H_2O and quickly added to an aqueous ammonia solution (1 mL ammonia hydroxide aqueous solution, 25 %, +20 mL H_2O) under rigorous stirring. After enclosing the Teflon liners in steel autoclaves, autoclaves were placed in a furnace, respectively wrapped into a heating mantle system (equipped with a thermocouple K:Class:2 by Toho and a Program Temperature Controller TXN700 by AS ONE) and heated to a temperature of 200 °C that was kept for 6–12 h. In all cases, the obtained powders were collected by centrifugation, washed two times with distilled water and dried at 80 °C for at least 12 h. Crystalline oxide powders were obtained by post-thermal treatment at 900 °C (30 min).

2.2 Surface modification

For surface modification of $Gd_2O_3{:}Er^{3+},Yb^{3+}$ with PEG-*b*-PAAc, the nanostructures were dispersed in water (c = 2 mg/mL) and sonicated for 30 min at room temperature. An aqueous PEG-*b*-PAAc solution was added into the nanostructure dispersion, resulting in final concentrations of 0.6 mg/mL $Gd_2O_3{:}Er^{3+},Yb^{3+}$ and 0.6 or 1.2 mg/mL PEG-*b*-PAAc. In case of 0.6 mg/mL PEG-*b*-PAAc, 6 mg/mL PEG-6.000 have been added to the aqueous nanostructure dispersion prior to addition of the PEG-*b*-PAAc solution in order to increase viscosity of the reaction mixture hindering the formation of larger agglomerates. The mixtures were stirred at 35 °C for 24 h. The obtained surface modified powders were collected by centrifugation, washed at least three times with distilled water and dried at room temperature.

2.3 Material characterization

The crystalline phase of the samples was determined by powder XRD with a ULTIMA III diffractometer (Rigaku) using CuKα radiation. Morphology of the obtained powders was investigated by scanning electron microscope (S-4200, Hitachi). The size distribution of PEG-*b*-PAAc modified powders in distilled water was measured by dynamic light scattering (DLS) using a Dynamic Light Scattering Particle Size Analyzer LB-550 by Horiba. For FT-IR spectroscopy, samples were mixed with KBr and spectra of the powders were recorded under vacuum conditions using a JASCO FT/IR-6500 spectrometer. Upconversion emission spectra were recorded at room temperature using a RF-5000 Spectrofluorometer by Shimadzu-Seisakusho under excitation by an IR diode laser at 980 nm. For near infrared emission samples were excited at room temperature with the aid of a Laser Diode by Kamamatsu Photonics K. K. (L9418-04, $\lambda_P = 977.7$ nm) using a Thorlabs Laser Diode Controller 2A (LDC 220), Temperature Controller (TED 200) and Laser Diode Mount (6 mm/9 mm). Near infrared emission was detected with a detection system Avantes (AvaSpec-NIR 256-1.7, NIRA, set for 969–1750 nm, Slit-50). In order to investigate chemical durability under acidic conditions bare and PEG-*b*-PAAc modified nanostructures were added into an aqueous HCl solution with an initial pH of 3.0 ($c(Gd_2O_3) = 0.2$ mg/mL). Under rigorous stirring, the time-dependent change of pH was recorded by use of an Auto Titrator Com-1600 (Hiramura). The zeta-potential of bare and PEG-*b*-PAAc modified nanostructures was determined with a DelsaTM Nano Submicron Particle Size and Zeta Potential analyzer by Beckman Coulter using the disposable cell for zeta-potential unit. Therefore, nanostructures were suspended (0.67 mg/mL) in distilled water (pH = 5.2) or in an aqueous solution of NaOH with an adjusted pH value of 7.3 (corresponding to the pH value of cell culture medium). The zeta-potential was calculated from the mobility by the equipment's software using the Smoluchowski model.

2.4 Cytotoxicity tests

B-cell hybridomas (cell line: 83-12-5, purchased by ATCC, CRL-1971) and macrophages (cell line: J774, purchased by ATCC, TIB-67) were used to evaluate cytotoxicity of the obtained nanostructures using in vitro experimental protocols. B-cell hybridomas and macrophages were cultured in RPMI 1640 medium (Sigma-Aldrich) containing 10 % FCS, 2-mercaptoethanol (2ME), 2 mM L-glutamine, penicillin/streptomycin, 0.1 mM HEPES, 0.1 mmol/L non-essential amino acid and 1 mmol/L pyruvic acid for 24 or 48 h with respective nanostructures. Before incubation, the nanostructures were sterilized by use of 70 % ethanol and afterwards the nanostructure culture medium mixture was sonicated for 5 min. Concentrations of the nanostructures in the cell culture media varied between 1 and 500 μg/mL. Viability of B-cell hybridomas and macrophages was analyzed with trypan blue dye-exclusion assay by counting cells in a hemocytometer.

As positive control the anti-cancer drug carboplatin (c = 100 μg/mL, provided by Nihonkayayaku) was used, which is known to induce cell death [39]. Incubation in cell culture medium without nanostructures demonstrated the negative control simulating cell behavior under ideal conditions. All data obtained for incubated nanostructures were compared to the untreated control.

2.5 Staining and fixation of macrophages for in vitro CLSM investigations

In order to stain the cytoplasm of macrophages, macrophages were incubated for 10 min with 1 μM of CellTracker Orange 5-(((4-chloromethyl)benzoyl)amino) tetramethylrhodamine (CMRA) (invitrogen) according to the manufacturer's instructions. CMRA labelled macrophages were then incubated for 12 h with 500 μg/mL $Gd_2O_3:Er^{3+},Yb^{3+}$. The incubated cells were fixed with 4 % PFA, permeabilized with 0.1 % Triton-X-100 and the nucleus was stained with DAPI (1 μg/mL). CMRA and DAPI stained macrophages were enclosed between glass slides for further microscopy analysis. The applied analysis combined CLSM with the measurement of the multi-photon-absorption-induced luminescence from the used nanoparticles according to Farrer et al. [40]. The analysis was carried out using an Axiovert 200 M microscope including a 510 NLO Meta device (Zeiss, Jena, Germany) with helium-neon and femtosecond Ti-sapphire laser (Chameleon, Coherent, Santa Clara, CA). For DAPI detection a two photon excitation with 760 nm tuned Chameloen laser was used. The CMRA was excited at 543 nm using helium–neon laser. For nanoparticle or nanorod detection the chameleon laser was tuned at 980 nm to excite erbium and ytterbium ions. The laser pulse had a repetition rate at 80 MHz and the emission was collected with a 40× oil-immersion objective and a bandpass filter with a transmission window from 500 to 550 nm for the green signal (550 nm) or a bandpass filter from 650 to 710 nm for the red luminescence (670 nm). All pictures were taken within the inner section of the cells and the software LSM Image Examiner was used for further analysis.

2.6 In vivo distribution in mice organs

In order to study the in vivo distribution of the nanostructures, the mice were injected with 500 μL of $Gd_2O_3:Er^{3+},Yb^{3+}$ nanoparticles or nanorods in HEPES buffer (20 mM, pH = 7.4, 150 mM NaCl) through the tail vein [nanostructure concentration at the injection point at the tail vein: $c(Gd_2O_3:Er^{3+},Yb^{3+}) = 5$ mg/mL, 2.5 mg per mouse]. Day-0-mice were killed a few hours after injection. Day-1-mice were killed 24 h after injection. After removing the hair of the mice by using commercial depilatory, mice were observed in the "1000-nm NIR in vivo fluorescence bioimaging" (OTN-NIR-IFBI) system NIS-Opt by Shimadzu equipped with a 980-nm laser diode (S4LFT0101/126 SILL155129), a scanner for the fluorescence excitation and an InGaAs-CCD (Xenics Detector), which can detect the image in between 800 and 1,700 nm (Scheme 1). Uniformity of the laser intensity is achieved by using a scanning galvanometer mirror system that allows scanning the whole mouse body (centimeter range). Near-focus was chosen for the incident laser beam on the animal in order to avoid burning of the biological tissue. The laser power was set to be 4.5 W with a ΨAmaki LD Driver & Temperature Controller.

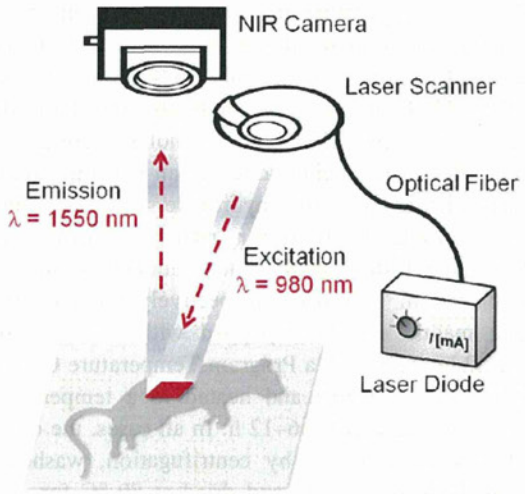

Scheme 1 Schematic representation of the "1000-nm NIR in vivo fluorescence bioimaging" (OTN-NIR-IFBI) system NIS-Opt

For histological analysis in fluorescence microscope (IX71 by Olympus, equipped with a near infrared source TCLDM9 by Thorlabs), organ samples (liver, spleen, lung, kidneys) were fixed with 10 % formalin and histological evaluation was performed using hematoxylin and eosin (H&E) staining. Urine from day-0 and day-1-mice injected with 85 and 160 nm particles could be collected while sacrificing and was also investigated in fluorescence microscope for residual nanostructures. NIR emission intensity was quantified (integrated density) by greyscale analysis of the obtained fluorescence micrographs using the software ImageJ. Experiments were done under the detection systems' pixel saturation limit (further information and discussion on the lower detection limit and pixel saturation of the used NIR camera systems are provided in Supporting information).

3 Results and discussion

3.1 Material synthesis and characterization

3.1.1 Phase and morphology

Hydrothermal treatment (HT) and HP methods such as surfactant-free HP, CTAB-assisted HP as well as CTAB- and PEG-6.000-assisted HP were used for the synthesis of various Ln^{3+}-doped gadolinium based nanostructures.